



## Article

# Assessing Impacts of Flood and Drought over the Punjab Region of Pakistan Using Multi-Satellite Data Products

Rahat Ullah <sup>1,2,3</sup>, Jahangir Khan <sup>4,5</sup>, Irfan Ullah <sup>6</sup> , Faheem Khan <sup>7,\*</sup> and Youngmoon Lee <sup>8,\*</sup>

- <sup>1</sup> Institute of Optics and Electronics, Nanjing University of Information Science & Technology, Nanjing 210044, China
  - <sup>2</sup> Jiangsu International Joint Laboratory on Meteorological Photonics and Optoelectronic Detection, Nanjing University of Information Science & Technology, Nanjing 210044, China
  - <sup>3</sup> Jiangsu Key Laboratory for Optoelectronic Detection of Atmosphere and Ocean, Nanjing University of Information Science & Technology, Nanjing 210044, China
  - <sup>4</sup> Key Lab of Remote Sensing for Agri-Hazards, Ministry of Agriculture, College of Information & Electrical Engineering, China Agricultural University, Beijing 100083, China
  - <sup>5</sup> Department of Computer Science & Information Technology, Sarhad University of Science & Information Technology, Peshawar 25120, Pakistan
  - <sup>6</sup> College of Hydrology and Water Resources, Hohai University, Nanjing 211100, China
  - <sup>7</sup> Department of Computer Engineering, Gachon University, Seongnam-si 13120, Republic of Korea
  - <sup>8</sup> Department of Robotics, Hanyang University, Ansan 15588, Republic of Korea
- \* Correspondence: faheem@gachon.ac.kr (F.K.); youngmoonlee@hanyang.ac.kr (Y.L.)

**Abstract:** The Punjab region of Pakistan faced significant losses from flash flooding in 2010 and experienced a multiyear drought during 1998–2002. The current study illustrates the drought and flood conditions using the multi-satellite data products derived from the Moderate Resolution Imaging Spectroradiometer (MODIS) and Tropical Rainfall Measuring Mission (TRMM) as well as the TRMM Multi-satellite Precipitation Analysis (TMPA) satellites with high-quality resolution in the region of Punjab during 2010–2014. To determine the drought and flood events, we used the Vegetation Temperature Condition Index (VTCI) drought monitoring approach combined with the Normalized Difference Vegetation Index (NDVI) and Land Surface Temperature (LST) to identify the warm and cold edges (WACE) in the provision of soil moisture as well as the VTCI imagery using the MODIS-Aqua data products. We assessed the 2010 flood effect on the four years (2011–2014) of drought conditions during winter wheat crop seasons. The obtained VTCI imagery and precipitation data were utilized to validate the drought and flood conditions in the year 2010 and the drought conditions in the years 2011–2014 during the winter-wheat-crop season. It is worth mentioning that over the four years (2011–2014) of the Julian day~D-041 year, the VTCI shows a stronger link with the accumulative precipitation anomaly ( $r = 0.77$ ). It was found that for D-201 during the 2010 flood was the relationship was nonlinear, and in D-217, there was a negative relationship which revealed the flood timing, duration, and intensity. For D-281, a correlation ( $r = 0.97$ ) was noted during fall 2010, which showed the drought and flood extreme conditions for the winter-wheat-crop season in the year 2010–2014. In regard to 2010, the Global Flood Monitoring System (GFMS) model employs the TRMM and TMPA data products to display the study region during the 2010 flood events and validate the VTCI results. This study's spatial and temporal observations based on the observed results of the MODIS, TRMM, and TMPA satellites are in good agreement with dry and wet conditions as well as the flood runoff stream flow and flood intensity. It demonstrates the flood events with high intensity compared with the normality of flood with the complete establishment of flood events and weather extremes during the year of 2011–2014, thereby highlighting the natural hazards impacts. Our findings show that the winter wheat harvest was affected by the 2010 monsoon's summer high rain and floods in the plain of Punjab (Pakistan).

**Keywords:** drought; flood; GFMS; MODIS; VTCI; Pakistan



**Citation:** Ullah, R.; Khan, J.; Ullah, I.; Khan, F.; Lee, Y. Assessing Impacts of Flood and Drought over the Punjab Region of Pakistan Using Multi-Satellite Data Products. *Remote Sens.* **2023**, *15*, 1484. <https://doi.org/10.3390/rs15061484>

Academic Editors: Hongxing Zheng and Ruirui Zhu

Received: 4 December 2022

Revised: 28 February 2023

Accepted: 1 March 2023

Published: 7 March 2023



**Copyright:** © 2023 by the authors. Licensee MDPI, Basel, Switzerland. This article is an open access article distributed under the terms and conditions of the Creative Commons Attribution (CC BY) license (<https://creativecommons.org/licenses/by/4.0/>).

## 1. Introduction

Pakistan is a South Asian country where the soil moisture (SM) and precipitation data provide insufficient information to detect drought and flood. The reason is the deficiency of reliable and comprehensive data, appropriate information network systems and rain gauges, as well as less accessible radar systems, especially in the Punjab region of Pakistan [1,2]. Satellite remote-sensing technology is used to monitor meteorological droughts, agricultural droughts, and flood events by mapping the imagery of the earth's surface over various wavelengths [3–5]. This provides a synoptic view of the land with a spatial environment for estimating the multilevel (global to local) applications [6]. The remote-sensing datasets are available for extensive development, analysis, determination, and validation, and their application in addressing the key challenges of earth observatory systems (EOS) is an open debate [3,7]. The remote-sensing data products are easy to use in terms of compatibility and accessibility, especially for detecting land cover changes [7]. In addition, satellite-based global precipitation data contribute to determination, validation, forecasting applications, and weather and climate studies [3]. The sensor chosen for this investigation, the Moderate-Resolution Imaging Spectroradiometer (MODIS), uses 36 spectral bands in the range ~0.4–14.4  $\mu\text{m}$  to cover all landforms on earth in a single or two-day period [3,7]. Limited satellite-driven indices have developed considerably for monitoring in the long term [8–11]. The important use of remote-sensing technologies for essential processes of demodulating and monitoring droughts and flood events must be actively investigated [12].

Drought is a subtle and creeping hazard that results from meager annual precipitation and has a negative impact in multiple areas, such as the world's agricultural, atmospheric, ecological, and socio-economic spheres [11,13–16]. Accurate drought assessment and monitoring strictly rely on the rainfall measurement in a specific region as well across the globe for drought monitoring and flood detection [9,10]. To investigate and monitor drought and flood, various indices have been proposed [13,16,17] that reflect comprehensive information based on meteorological, agricultural, and hydrological components/variables (i.e., drought conditions, SM, surface water runoff, stream flow) regionally and globally [14,18–21].

Among the conventional meteorological indices, time and space comparisons of drought severity are possible under the established meteorological conditions within reasonable limits through quantities such as the standardized precipitation index (SPI) and Palmer Drought Severity Index (PDSI) [16,22]. SPI was used to represent antecedent SM deficit and moisture supply [23]. In the U.S., the PDSI, Palmer Hydrological Drought Index (PHDI), Palmer Modified Drought Index (PMDI), and Palmer Z-Index are used to measure drought conditions [15,16,24,25]. The PDSI is a practical tool that makes use of temperature and precipitation information to estimate the relative dryness and wetness that is suitable for the long-term quantification of drought. The PDSI limits the primary impact of climate change on drought by altering potential evapotranspiration [18,19]. Therefore, Dai (2013) assessed the hydro-meteorological indices such as SPI and PDSI for aridity changes and streamlined several significant problems. These problems led to new indices that detect more diverse forms of SM and drought [26,27].

Recently, Zeng and Lu [28] presented the interesting potential of monsoon onset and retreat to facilitate the diagnostics and validation of global monsoon replications. The monsoon inception pattern for summer is associated with the dry-to-wet evolution, with a time series and retreat dates from seasonal cycles that cause natural hazards (i.e., drought and flood) [10]. Due to monsoon rains in summer, SM and rainfall had a significant association, and therefore, SM plays a considerable role in maintaining drought or flood conditions through the summer season [10,29,30]. Lu (2009) used a weighted average of precipitation (WAP) to determine the inter-annual variabilities and long-term changes of the start, duration, and strength of flood and drought. However, there are limitations to drought monitoring and flood detection using SPI, which can determine the general level flood and drought for several months or years but cannot be used for short scales (e.g., a

week or less). Hence, SM plays a significant role in maintaining drought or flood conditions during the summer [29,31].

The remote-sensing indices that are very comparable and used in our research are land surface temperature (LST) and normalized difference vegetation index (NDVI). Many studies incorporate and utilize the NDVI and LST for drought monitoring, SM, and flood detection [2,9,10,32]. Many indices such as the temperature vegetation dryness index (TVDI), water deficit index, crop water stress index, and vegetation temperature condition index (VTCI) have been defined for quantification of drought conditions and near-real-time monitoring with spatial drought amount [11]. Bai et al. [33] used the MODIS NDVI and LST products for drought and SM extraction in consideration of the TVDI and crop water stress index in the Guanzhong Plain of China. The normalized difference water index was considered for monitoring vegetation state and health, along with the normalized multi-band drought index for monitoring SM [34,35]. Furthermore, indices such as the standardized vegetation index incorporate the NDVI and, for a short period, observe drought in terms of poor vegetation [36]. In addition, the meteorological Z-score (Z), China-Z index, and modified China-Z index drought indices were evaluated in comparison with the remote-sensing perpendicular drought index and modified perpendicular drought index by incorporating the MODIS data product for drought monitoring [9]. In addition, Parviz [37] investigated the NDVI, vegetation condition index, temperature condition index, enhanced vegetation index, vegetation health index, temperature vegetation index, normalized vegetation supply water index, and VTCI for drought monitoring and established significant results with more efficiency in utilizing the remote-sensing indices based on the combination of vegetation condition and LST, which together reflect the entire information regarding SM and drought.

The EOS's MODIS data products define the study of global change, which are more comprehensive for our studies of drought and flood events detection [37–39]. They provide effective high-resolution products in the optical range to determine the drought and flood events in the region of Punjab, Pakistan. In addition, VTCI is a superior method to the combined LST and NDVI for detecting the margins, drought, and flood in the area. It can be utilized together with data on flood occurrences, drought conditions, and SM of the land surface [24,32]. The LST and NDVI spatial patterns can be deployed to identify the warm and cold edges (WACE) (LST max and LST min), also called 'dry-edge' and 'wet-edge' (e.g., Zhou et al. The authors of [40] present global transformations in land surface SM conditions and approximate changes in vegetation to determine the relative parameters and provide information for robust agricultural practices in China [3,7,24]. Further, Han et al. [41] employed the MODIS data products of LST and NDVI to investigate SM in the greater Changbai Mountains, utilizing the TVDI using the wet-edge and dry-edge in relationship to reveal temporal changes in the land surface SM conditions. Variations in SM lead to significant changes in land surface climatology, energy balance, hydrology, and vegetation in the evaluation of ecology environment conditions (e.g., climate, land use, soil, temperature, and vegetation) and atmospheric processes [41–43]. Furthermore, Wan et al. [24] and Sun et al. [32] employ VTCI in the U.S. and China for the monitoring of both drought conditions and WACE, respectively, indicating that the employment of LST and NDVI might be effective with our VTCI approach in the plain region of Punjab (Pakistan).

Therefore, it is important to explore the region and its associated events using the VTCI drought monitoring approach to determine the dry and wet conditions. We also employ the Global Flood Monitoring System (GFMS) model for the flood detection/intensity and stream flow during the year of 2010 over Punjab, Pakistan. The VTCI approach is considered in our study to investigate the drought during 2011–2014 and the drought conditions and floods in the year 2010. In addition, for the rationalization and validation of VTCI imagery in the 2010 flood results, we consider the GFMS model for the deluge plot time series on the region and each five stations based on time intervals during 2010 to determine the flood events, such as the flood stream flow, flood detection/intensity, and the precipitation anomaly over selected stations. The validation of MODIS VTCI imagery for flood detection

during 2010 using daily precipitation data and the GFMS model-based flood events are quite consistent over the region. The GFMS quantitative information using the real-time Tropical Rainfall Measuring Mission (TRMM) and TRMM Multi-satellite Precipitation Analysis (TMPA) precipitation data product archive to determine flood events such as flood stream flow, flood detection/intensity and rainfall anomalies over the stations/region is very consistent with our MODIS VTCI results in the year 2010.

## 2. Study Area

The most cultivated province of Pakistan, Punjab, has faced the longest and most severe droughts during the last hundred years (1902–2002) and the devastating 2010 flood [44,45]. The foremost reason for the droughts in Pakistan is the shortfall of rain and flooding due to heavy rainfall events associated with monsoons approaching from the southwest, allied to La-Nina and El-Nino events [46–49]. Droughts are impacting the agriculture sector (through crop failure) and other sectors of the economy. During 2000–2001, agricultural growth was severely affected and declined. Due to severe drought, major crops such as wheat, cotton, and rice had productivity reduced to 10%, minor crops suffered severe setbacks due to long dry spells, and water shortages were up to 51% compared with 40% under normal conditions [50]. In addition, natural hazards such as floods in the downstream areas of the Indus River basin can cause misery for a flood-prone country such as Pakistan. The country faced the worst flood since its inception in 2010, which affected 24 million people in total, damaged more than 2 million hectares of crops, and caused 10 billion USD in economic losses [51].

Pakistan's cropping systems are based on cotton–wheat and rice–wheat rotations and cover three-fifths of the plain of Punjab. In these systems, 75% of the wheat crop is accompanied by berseem, with a 14% share, and 87% of the rice crop is accompanied by fodder, with an 8% share, in the Kharif and Rabi seasons, respectively [50,52]. Likewise, Punjab produces 85% of cotton in the country, and the Sindh province produces 15% of the total cotton crop of Pakistan, and the country is the fourth largest producer and consumer of cotton in the world. The Punjab plain crop rotation begins with sowing of the winter wheat crop in late October to early November, and the wheat is harvested in early to late April. In addition, the sowing of the cotton crop starts in the southern plain in late April, while in the northern plain, the sowing ends in early May, whereas the crop harvest takes place in early and late October in the plain [20,53].

## 3. Materials and Method

### 3.1. Datasets

In the current study, we used the MODIS Aqua (EOS PM) earth science 8-day LST (MYD11A2) data product with known emissivity in bands 31 and 32. The NDVI (MYD13A2) data product values were acquired over 16-day intervals at a spatial resolution in bands 1 and 2 to effectively distinguish the states and processes of vegetated surfaces. We used a sinusoidal grid with an approximately 1 km land product overlap and included the h23/v05, h24/v05, and h24/v06 tiles in the integrated sinusoidal projection. In response, two reflective bands, that is band-1 (red, 620–670 nm) and band-2 (near-infrared, 841–876 nm), and two emissivity bands, band-31 (10.780–11.280  $\mu\text{m}$ ) and band-32 (11.770–12.270  $\mu\text{m}$ ) are used to determine the land cover changes. The data can be found at <https://modis.gsfc.nasa.gov/> accessed on 22 December 2022 [7]. This study utilizes the MODIS temporal and spatial resolution at a 1 km pixel area (i.e., NDVI and LST data products) and the TRMM and TMPA temporal resolution (3 hourly) at relatively high spatial (~1 km) and flood stream flow at high spatial (~12 km) resolution during 2010. In addition, the meteorological measured daily precipitation data of five weather stations were obtained from the Pakistan Meteorological Department (PMD). Consequently, the two stations at Multan (i.e., MLN1 and MLN2) are located in the south, and two stations are located in the center at Faisalabad (i.e., FSD1 and FSD2), whereas LHR is located in the northeast part of the plain of Punjab, with each station having a certain elevation, latitude and longitude [8]. The available

precipitation data for the five stations with three climatic divisions (south, center, and northeast) of Punjab are considered using the daily precipitation data in certain periods (TPCPi) from 16-days to one-year, spanning 2010–2014. These data are considered with the MODIS VTCI imagery from January first-sixteen days (D-009) to June first-sixteen days (D-169) during 2011–2014. Similarly, the cumulative precipitation from 16-days to one-year spanning 2009–2010 is used with the MODIS VTCI imagery during 2010 from January first-sixteen days (D-009) to December last-sixteen days (D-361) to validate the drought and flood events in the year 2010. Therefore, our research presents the VTCI imagery day (D) of years in line with Julian Day (JD) to determine and validate the given time series. A linear correlation analysis is applied to study the relationship between precipitation and VTCI imagery at particular stations. Hence, for this study, the measured ground precipitation anomaly is considered in millimeters (mm) for the validation of the VTCI (i.e., NDVI and LST) data products over the five weather stations of the Punjab region.

### 3.2. Methods

A sinusoidal projection is examined for the emissivity values per pixel area in a sequence of swath-to-grid-based global products from MODIS-Aqua. The data are produced at ~1 km spatial resolution on the geographically aggregated LST over 8-day intervals, whereas the NDVI (ratio of red and near-infrared reflectance) data products span 16-day intervals in a certain period, which provides continuity for time-series applications in this study. LST and NDVI combine factual information to characterize and quantify SM, drought, and flood events [54,55]. Trapezoidal space graphs of the LST and NDVI have been proposed for describing quantitative metrics of SM [24,32,56,57]. Previously, the coupling of LST and NDVI data through the method called maximum value compositing (MVC) and the VTCI approach were employed for monitoring drought in the U.S. and China [32]. In another study, Sun et al. [32] proposed the MVC approach by coupling the advanced, very high-resolution radiometer (AVHRR) LST and NDVI products in certain periods to determine WACE and drought in the Guanzhong plain of China.

Based on our findings, we selected the MVC technique as the maximum–minimum-value compositing strategy, which was conclusively resolved by the consistent use of maximum-value composite annual and multiyear LST and NDVI products. The edges can be calculated in one of three ways: (1) using the maximum values from each year's merged LST and NDVI products in the relevant time period; (2) using the multiyear maximum values from these same sets of products in the relevant time period; or (3) using the multiyear maximum–minimum values from the composite LST and NDVI products to calculate the warm edge and the multiyear maximum-value sets and calculate the cold edge [24,32,58]. The MVC method ensures an NDVI value with a better agreement in the case of over-estimation of the vegetation biophysical parameters and contributes to the saturation of the NDVI for coupling in retrieving the soil surface and atmospheric properties to improve the LST salvage [30].

The VTCI plots in the LST-NDVI space are useful for detecting droughts and WACE in SM. The processed data for WACE is in parallel to the NDVI axes and in relation to NDVI, respectively [24]. In VTCI's time series, the LST-NDVI feature space, also known as the triangular or trapezoidal region, displays the vegetation as well as soil thermal content as LSTmax and LSTmin, the distinctions of vegetation, temperature, and the changes in time/seasons. The slope of the warm edges' absolute values on the LST-NDVI space plot is in line with differences in temperature and area-specific soil characteristics. Based on the integration of both the LST and NDVI data products and the use of a single year's maximum values in response to WACE over a predetermined period, VTCI drought imagery and SM are determined. With a particular NDVI's value in a defined area, the VTCI can determine the ratio of differences among LST's pixels, as given below:

$$VTCI = \frac{LST - NDVI_{i_{\max}} - LST - NDVI_i}{LST - NDVI_{i_{\min}} - LST - NDVI_{i_{\min}}} \quad (1)$$

where:

$$LST - NDVI_{i_{max}} = a + bNDVI_i \quad (2)$$

$$LST - NDVI_{i_{min}} = a' + b'NDVI_i \quad (3)$$

Hence,  $LST - NDVI_{i_{max}}$  and  $LST - NDVI_{i_{min}}$  represent the LST of pixels with alike  $NDVI_i$  values in the study region.  $LST - NDVI_i$  shows the LST of a single pixel with an  $NDVI_i$  value. Here  $a, b, a',$  and  $b'$  show the coefficients that can be estimated from a larger area whose SM at the surface layer spans from the wilting point to the field capacity at the pixel level. Typically, the dispersed LST and NDVI plots are used to determine the coefficients. The above equations define the preliminary judgment indicators in the form of scatterplots (soil, moisture, and droughts). Further, the four given coefficients ( $a, b, a',$  and  $b'$ ) evaluate the assessed VTCI space plot of the LST dissension midst pixel with an exerting and distinctive influence with NDVI accounting for the comprehensive region expansion. The observed surface temperature at a given pixel of LST is calculated in kelvin 'k'.

The NDVI can be given as:

$$NDVI = \frac{\rho_{NIR} - \rho_{red}}{\rho_{NIR} + \rho_{red}} \quad (4)$$

where  $\rho_{red}$  and  $\rho_{NIR}$  are the MODIS reflectance bands 1 and 2 with a range of 620–670 nm and 841–876 nm, respectively. This helps in finding the wetness of soil in the shallow horizon, and the extent of wilting sites regionally and geospatially at the pixel level of the NDVI-LST space plots.

The studies in [24,32] utilized the remotely-sensed LST and NDVI feature space as trapezoidal shapes using the MVC method to identify the edges for single and multiple years. The dry and wet edges represent pixel values from zero to one in the feature space of LST/NDVI to signify the SM contents and, in response, result in the VTCI imagery in every single year with 16-day intervals in the given period/s. The VTCI drought monitoring method unites the remotely observed radiant fluxes according to a particular thermal value and wavelength. It provides a transition using the NDVI and LST. The VTCI drought monitoring yields different results at different time scales, and the scale of 16-days was selected in our study as it is more promising and practical [58]. The VTCI scores were then classified into four distinct levels of drought severity: wet or normal conditions (0.57 to 1.0), minor (0.57 to 0.44), moderate (0.44–0.38), and extreme drought (0.38 to 0). For validating the VTCI imagery of drought and flood uses, the pixel areas within a certain range are considered with the daily on-ground precipitation information at certain periods over five weather stations. The accumulative precipitation data are set to the accumulative precipitation anomaly (TPCP), and their combinations for 16 days, 1-, 2-, 3-, 4-, 5-, 6-, 9-, and 12-month intervals with VTCI imagery from January's first 16 days to the first 16 days of June during 2011–2014. Similarly, the TPCP intervals are considered with the VTCI imagery from January's first 16 days to December's last 16 days during 2010:

$$VTCI = A_i TPCP_i \times B_i \quad (5)$$

where  $TPCP_i = \sum_{i=1}^n TPCP_i$

VTCI is defined as the difference of  $(LST - NDVI_{i_{max}} - LST - NDVI_i)$  and  $(LST - NDVI_{i_{max}} - LST_{NDVI_i_{min}})$ . TPCP<sub>i</sub> shows the accumulative precipitation from 16 days to 12 months. A shows the slope/gain, and B presents the offset in the above equation. The VTCI imagery values from D-009 to D-169 are combined with TPCP from 16 days to 1 year during 2010–2014 in specified periods; similarly, the VTCI imagery values from D-009 to 361 during 2010 are combined with TPCP from 16 days to one year during 2009–2010 in specified periods, based on the linear-regression presented in Equation (5). Therefore, in the linear-correlation analysis, the VTCI imagery values are based on recent and past precipitation.

Typically, the MODIS VTCI's imagery from D-009 to 169 during the period of 2011–2014 and D-009 to 361 in the year 2010 is geospatially coupled in a relationship with the accumulative precipitation anomaly (TPCPI) in the periods (16-days, 1-, 2-, 3-, 4-, 5, 6-, 9- and 12-months) during 2010–2014 and 2009–2010, respectively. The precipitation anomaly is used in a matrix form for the validation of drought and flood events in specified periods. The GFMS/Drive model has been implemented for real-time application using the University of Washington Land Surface Model and a new physically based DRTR routing model from the University of Maryland for more accurate flood calculation and greater flexibility [59]. The GFMS is running quasi-globally (50°S–50°N) every three hours at 1/8th degree, and routing is also running at a 1 km resolution. According to the method by Wu et al., 2012 to detect flood events, the GFMS model using the TMPA-driven retrospective simulation for each grid cell remains determined as flooding at a time step. If the streamflow ( $Q$ ,  $m^3/s$ ) is greater than the flood threshold, i.e.,  $Q > P95 + \sigma$  and  $Q > 10$ , where  $P95$  and  $\sigma$  are the 95th percentile values and the temporal standard deviation derived from the retrospective simulation. Flooding occurs at a point if  $R > P95 + \delta$  and  $Q > 10 m^3/s$  ( $R$ : routed runoff (mm);  $P95$ : 95th percentile value of routed runoff;  $\delta$ : temporal standard deviation of routed run-off;  $Q$ : discharge ( $m^3/s$ )), employing the method of Wu et al., 2012 [44]. Thus, this study used the GFMS model to detect the flood intensity during 2010 across the target region. Detailed information about the data and method can be seen in Figure 1.

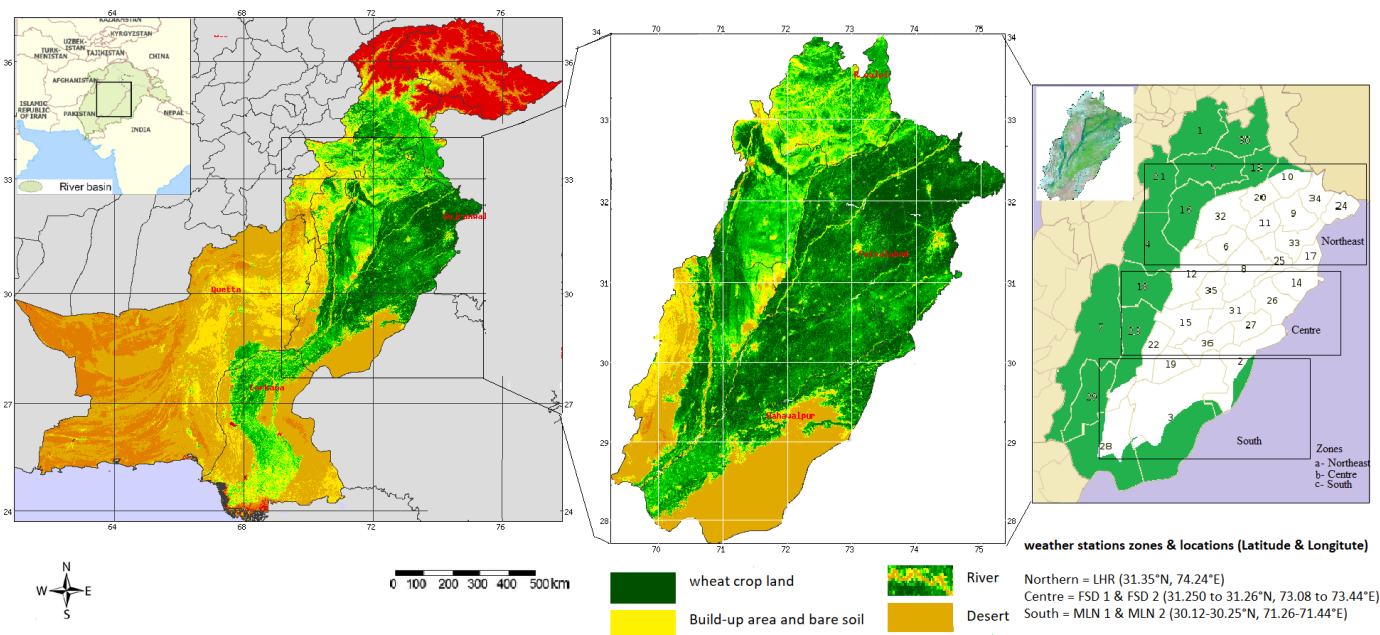


**Figure 1.** Geographical position with a sinusoidal grid over h23/v05, h24/v05, and h24/v06 mapped plates and pixel size with an approximately 1 km land product defined and coordinated (27.41–34.02°N, 69.15–75.23°E) with weather station zones located in the northern, central and southern parts of the Punjab region.

## 4. Results and Discussion

### 4.1. VTCI Drought, Warm and Cold Edges

The feature space plot of LST and NDVI products in the defined area is negatively correlated in a trapezoidal shape. It presents the warm edge and cold edge as SM for multiyear values in the given period without VTCI drought imagery, as presented in Figure 2a,b. In contrast, the coupling of LST and NDVI present the WACE in term of SM (Figure 3c–f) to construct the VTCI drought imagery using the single-year composite values of LST and NDVI in the given period, as shown in Figure 3a–d. At the extensive scale, warm edges resulted using multiyear maximum values, whereas using composite products of LST-NDVI for multiyear maximum–minimum values resulted in the detection of cold

edges in the D-041 from D-009 to 169 during 2011–2014 (see Figure 2a,b). The composite of LST-NDVI for a single-year maximum value to determine the WACE in the D-041 during 2011, 2012, 2013, and 2014 is presented in Figure 2c–f, and the response in the VTCI drought imagery is presented in Figure 3.

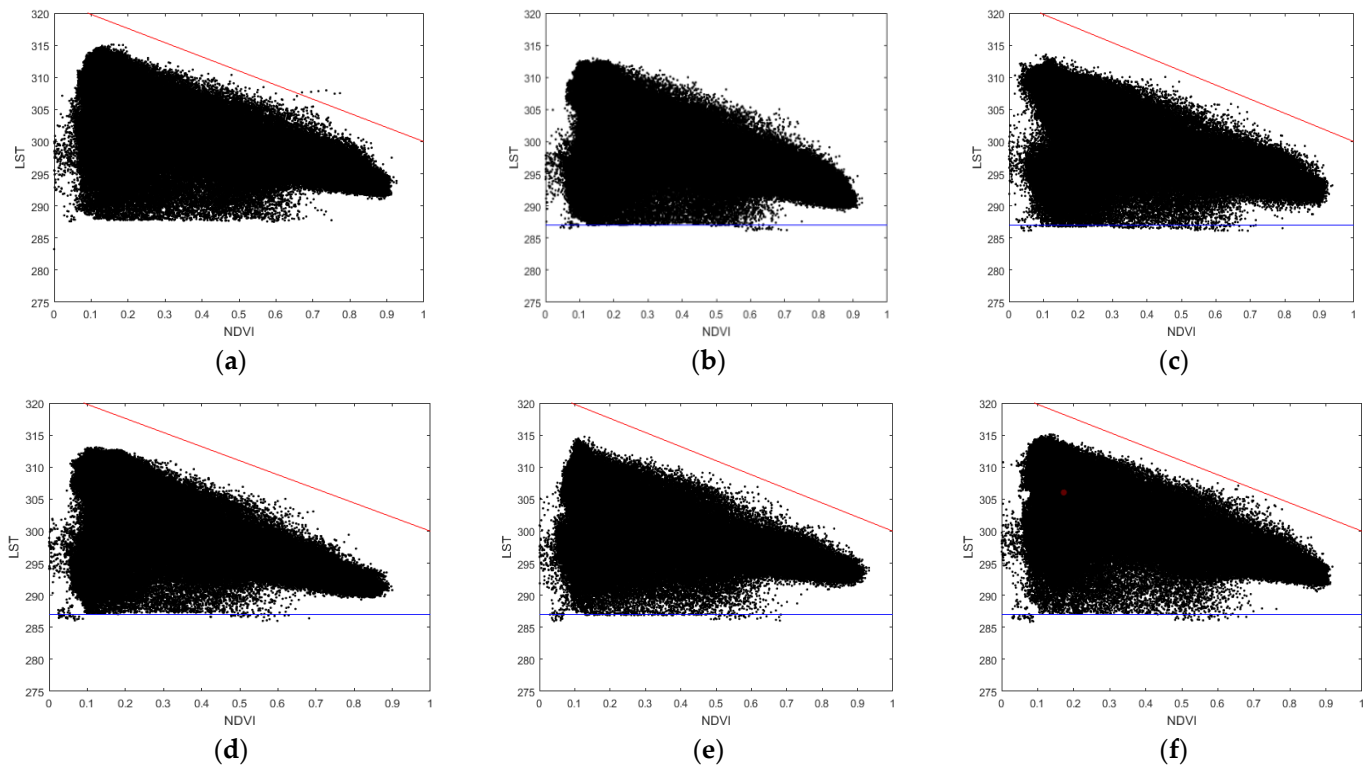


**Figure 2.** Scatterplots of LST and NDVI in the first 16 days of February (D-041) spanning 2011–2014: (a) Determining the cold edge using the multiyear maximum value NDVI products and maximum–minimum value composite LST products. (b) Determining the warm edge by the multiyear maximum value composite LST and NDVI products. (c–f) show the WACE plotting of the single-year maximum-value composite LST and NDVI products in the first 16 days of February (D-041) for the years 2011, 2012, 2013, and 2014, respectively.

In Figure 2, the warm edge regarded as LSTmax responds with less availability of SM and is under dry conditions, while the cold edges regarded as LSTmin present no water restriction for plant growth. In Table 1, warm–cold edges are utilized from D-009 to 169 for a single-year and multiyear during 2011–2014 and from D-009 to 361 for a single-year period during 2010. The WACE for more than one year at D-041 during 2011–2014 are presented in Figure 2a,b, and the WACE for single-years at D-041 in the years 2011, 2012, 2013, and 2014 are presented in Figure 2c–f, respectively. For further processing, Table 1 demonstrates variations in WACE for single and multiyear values during the winter wheat crop season in the 2011–2014 period and during all seasons in the 2010 period, respectively, and demonstrates the time/seasons in the region in response to WACE. Consequently, the determined warm and cold edges vary with weather extremes and natural processes in the form of SM dissimilarity and drought imagery.

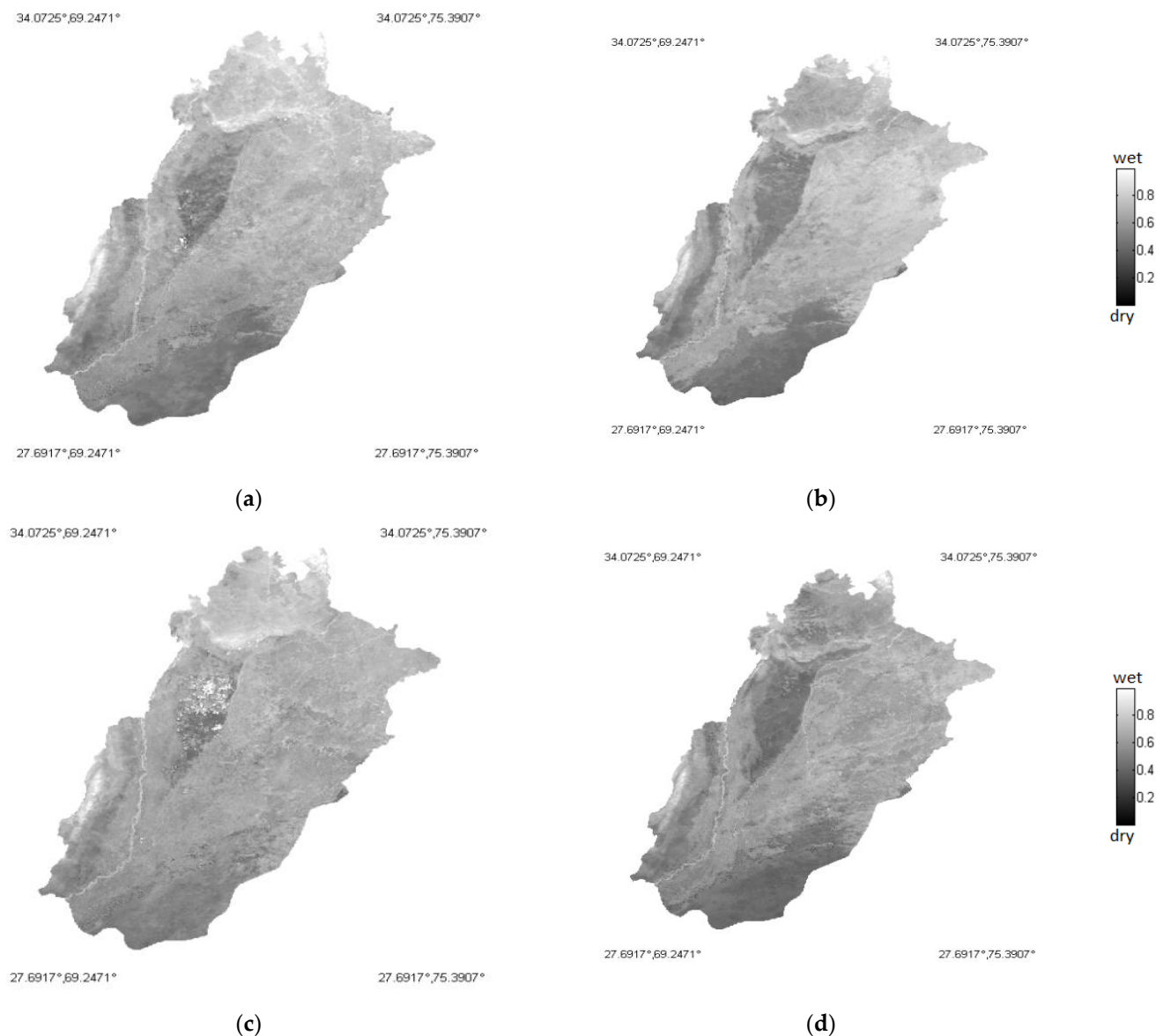


**Figure 3.** VTCI times series values reveal the dry and wet conditions on the VTCI fractional scale (dry to wet) or (0.0–1.0) in the region in the first 16 days of February (D-041) in a single-year maximum value of composite LST and NDVI products to determine the warm edges and cold edges during 2011–2014. This yields the MODIS VTCI drought imagery: (a) in 2011, (b) in 2012, (c) in 2013, and (d) in 2014. During the growing season for the winter wheat crop in D-041, 2011–2014, these photos have a strong correlation with one another.

Increased temperatures are observed due to the climate changes from winter to summer season during 2011–2014 as well as in all seasons during 2010 (see Table 1 and Figure 2). Due to weather extremes and flood events during 2010 in the region discussed, the chronological changes of the land surface and SM conditions are categorized as normal for agricultural practice in the following 4-year period (2011–2014). Therefore, the retreat states of edges are stable and substantially normal for the region in the four years 2011–2014.

From 2011–2014, the D-041 period experienced a drought, as seen by the VTCI drought imagery depicted in Figure 3. This imagery was created by combining a single year’s maximum and minimum 16-day LST composite data products with a single year’s maximum 16-day NDVI data products. Figure 3a–d shows the normal drought condition on the VTCI fractional scale (dry to wet) or (0.0–1.0) in the given period.

**Table 1.** Equations for the warm edges and cold edges for single years and multiple years from D-009 to D-169 during 2011–2014 and single-year from D-009 to D-361 during 2010. Warm edges are the thermal boundary defined as LSTmax Gains and Offset. Zero gain in cold edges are defined as LSTmin from D-009 to D-169. Day of the year (D) is presented here as (DOY).

DOY	Cold Edges	Warm Edges
009	$LST_{NDVI_i \min} = 287 + 0 \times NDVI_i$	$LST_{NDVI_i \max} = 319 - 25 \times NDVI_i$
025	$LST_{NDVI_i \min} = 287 + 0 \times NDVI_i$	$LST_{NDVI_i \max} = 320 - 19 \times NDVI_i$
041	$LST_{NDVI_i \min} = 287 + 0 \times NDVI_i$	$LST_{NDVI_i \max} = 322 - 22 \times NDVI_i$
057	$LST_{NDVI_i \min} = 292 + 0 \times NDVI_i$	$LST_{NDVI_i \max} = 330 - 30 \times NDVI_i$
073	$LST_{NDVI_i \min} = 294 + 0 \times NDVI_i$	$LST_{NDVI_i \max} = 330 - 25 \times NDVI_i$
089	$LST_{NDVI_i \min} = 298 + 0 \times NDVI_i$	$LST_{NDVI_i \max} = 341 - 30 \times NDVI_i$
105	$LST_{NDVI_i \min} = 298 + 0 \times NDVI_i$	$LST_{NDVI_i \max} = 341 - 30 \times NDVI_i$
121	$LST_{NDVI_i \min} = 300 + 0 \times NDVI_i$	$LST_{NDVI_i \max} = 341 - 30 \times NDVI_i$
137	$LST_{NDVI_i \min} = 300 + 0 \times NDVI_i$	$LST_{NDVI_i \max} = 341 - 30 \times NDVI_i$
153	$LST_{NDVI_i \min} = 300 + 0 \times NDVI_i$	$LST_{NDVI_i \max} = 350 - 39 \times NDVI_i$
169	$LST_{NDVI_i \min} = 300 + 0 \times NDVI_i$	$LST_{NDVI_i \max} = 350 - 31 \times NDVI_i$
185	$LST_{NDVI_i \min} = 298 + 0 \times NDVI_i$	$LST_{NDVI_i \max} = 338 - 26 \times NDVI_i$
201	$LST_{NDVI_i \min} = 290 + 0 \times NDVI_i$	$LST_{NDVI_i \max} = 330 - 25 \times NDVI_i$
217	$LST_{NDVI_i \min} = 285 + 0 \times NDVI_i$	$LST_{NDVI_i \max} = 330 - 25 \times NDVI_i$
233	$LST_{NDVI_i \min} = 295 + 0 \times NDVI_i$	$LST_{NDVI_i \max} = 335 - 30 \times NDVI_i$
249	$LST_{NDVI_i \min} = 298 + 0 \times NDVI_i$	$LST_{NDVI_i \max} = 330 - 25 \times NDVI_i$
265	$LST_{NDVI_i \min} = 298 + 0 \times NDVI_i$	$LST_{NDVI_i \max} = 330 - 25 \times NDVI_i$
281	$LST_{NDVI_i \min} = 298 + 0 \times NDVI_i$	$LST_{NDVI_i \max} = 330 - 23 \times NDVI_i$
297	$LST_{NDVI_i \min} = 295 + 0 \times NDVI_i$	$LST_{NDVI_i \max} = 320 - 20 \times NDVI_i$
313	$LST_{NDVI_i \min} = 294 + 0 \times NDVI_i$	$LST_{NDVI_i \max} = 317 - 16 \times NDVI_i$
329	$LST_{NDVI_i \min} = 292 + 0 \times NDVI_i$	$LST_{NDVI_i \max} = 315 - 18 \times NDVI_i$
345	$LST_{NDVI_i \min} = 288 + 0 \times NDVI_i$	$LST_{NDVI_i \max} = 313 - 20 \times NDVI_i$
361	$LST_{NDVI_i \min} = 285 + 0 \times NDVI_i$	$LST_{NDVI_i \max} = 309 - 17 \times NDVI_i$

#### 4.2. Time Series Drought and Flood Determination

The determination of the VTCI time series has been utilized for drought monitoring and flood detection, using the maximum–minimum LST of a single-year of composited data sideways with maximum NDVI data to reveal the drought in a single year (Figure 3). The VTCI drought imagery results are compared with the 16-day LST–NDVI plot in terms of WACE in the D-009 to 169 period spanning 2011–2014, and D-009 to D-361 in 2010. The highly correlated VTCI drought imagery values in D-041 are presented in Figure 4. The VTCI time-series values of drought in the last 16 days of February (D-041) during 2011–2014 and in the first 16 days of January to the last 16 days of December (D-009 to 361) in 2010 for drought and flood are presented for five meteorological stations located in the south, central and northeast of the plain of Punjab (See Figures 4 and 5, respectively).

The values determined during the 2011–2014 drought and 2010 flood events are shown in Figures 4 and 5. These figures show the normal wetness in most of the plain at each weather station at D-041 during 2011–2014 based on the VTCI quantitative results, whereas during the year 2010, from D-009 to D-361, the VTCI values over the five weather stations varied from 0.28 to 1.0 and highlight the weather extremes in the form of severe drought and wetness. During the 2010 flood, the VTCI values at D-201 were 1.0 over five weather stations, and at D-217, over four stations, there were values of 1.0 except at LHR (Figure 5). These determined VTCI values during 2010 show the season and flood events (time, duration, and intensity). In contrast, the VTCI values are categorized as normal (0.586492375–0.775163399) in the blooming stage (early February to early March) in the winter wheat crop season during 2011–2014 (see Figure 4).

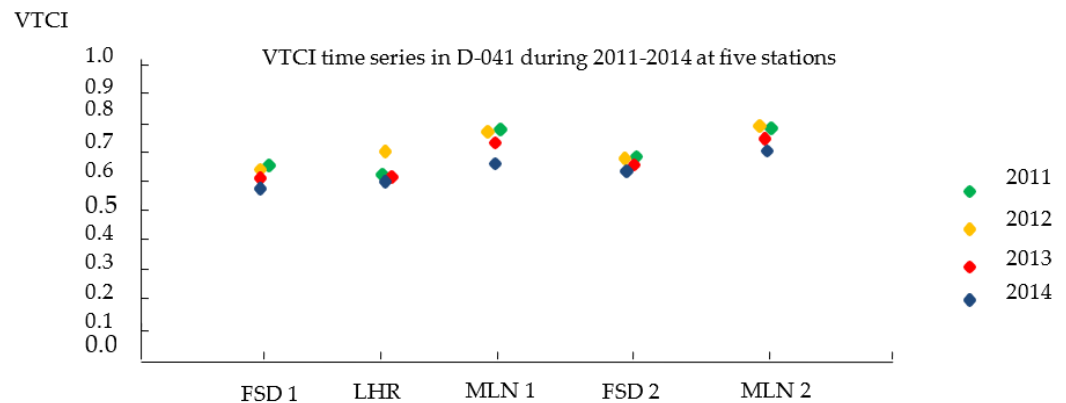


**Figure 4.** VTCI values for each of five meteorological stations in the D-041 period during 2011–2014 per pixel area of Punjab, based on the VTCI drought categorization. The presented VTCI categorization uses the following scales: wet to dry or 0 to 1; normality or wetness (1.0 to 0.57); and slightly mild (0.57 to 0.44), moderate (0.44 to 0.38), and severe (0.38 to 0.0) drought. The VTCI values in the first 16 days of Feb. (D-041) from 2011 to 2014 at five meteorological weather stations show the normality (0.586492375–0.775163399). The VTCI values at MLN 1 and MLN 2 present high values, whereas, FSD 1 and FSD 2 and the LHR have low VTCI values in the D-041 period. This shows that the area is not only rainfed but irrigated.

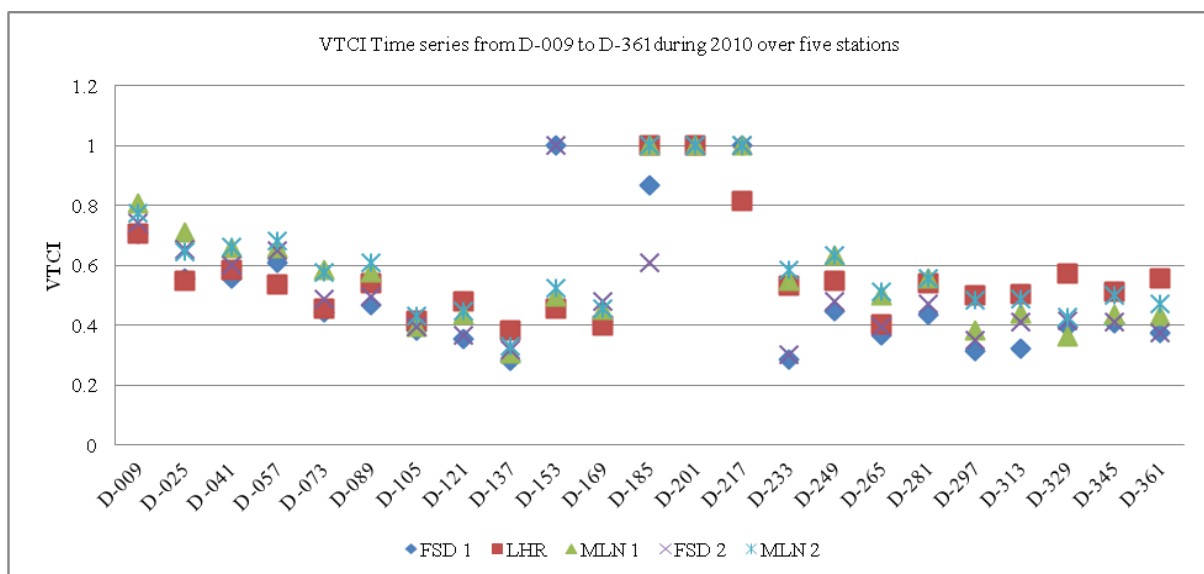


**Figure 5.** The VTCI values over five meteorological stations for days of the year (D-009 to D-361) during 2010 per pixel area on a scale of 0.0–1.0. The presented values show the drought, flood duration, and intensity (e.g., the values at D-185 indicate heavy rainfall, and values at D-201–232 indicate the flood duration, and intensity) at five stations over the Punjab region.

Moreover, the drought severity depends on the soil characterization: a lesser value of the VTCI can result in higher severity, whereas higher values of VTCI can result in normality or wetness, as shown in Figures 3–5. The determined VTCI drought values in D-041 during 2011–2014 show normality and did not include moderate or severe drought over the region at D-041 spanning 2011–2014 (Figure 4). Similarly, the drought values from D-009 to D-361 during 2010 varied from 0.28 to 1.0 on the fractional scale of 0.0–1.00 over the region (Figure 5). Considering the quantitative analysis of five stations during the 2010 period, we assumed the determined VTCI values from D-009 to D-361 over the five stations for drought and flood events. It was established that at D-185, heavy rainfall was recorded, and from D-201 to D-232, flood events (time, duration, and intensity) were observed over

five stations (Figure 5). Note that the VTCI drought and flood categorization are based on a fractional scale (0.0–1.0) or (dry to wet).

The results showed that severe droughts are not found throughout the winter wheat crop season in most of the southern, central, and northern Plain areas of Punjab. Adnan et al. [44] demonstrated that in Punjab, the northeast and west of the plain have variable precipitation in comparison with the southern part where most of the farms face inadequate rain compared with the northeast and north parts. In response, the accumulative precipitation does not show a relationship with some VTCI values over five stations from south to north. This indicates that this region is not fully dependent on the rainfall anomaly, indicating that the irrigation system in the region plays a significant role in the vegetation conditions.

Therefore, it is crucial when comparing and analyzing the two products, namely the VTCI values and TPCP anomaly, to characterize the land and determine the dependency on rainfall and irrigated practices over the plain of Punjab. Figure 4 shows our understanding of the VTCI drought throughout a four-year time frame at D-041 and across the board from D-009 to D-169 during the 2011–2014 winter and early summer seasons. The VTCI values ( $\sim n = 200$ ) observed on the plain in severe to wet conditions during 2011–2014 at each of the five sites ranged from 0.283 to 1.0. A total of 220 VTCI values were determined in the aforementioned analyses, and their drought severity was classified as severe ( $n = 11$ ), moderate ( $n = 18$ ), slight-mild ( $n = 79$ ), and normal ( $n = 112$ ). Figure 4 shows that the VTCI values at D-041 were relatively constant and showed a strong association with the TPCP anomaly during the years 2011–2014. Conditions ranging from severe drought to wet were also recorded across the plain from D-009 to D-361 in 2010 at the five sites, corresponding to 115 VTCI values (0.288 to 1.0). A total of 115 VTCI values were determined in the above-mentioned analyses, and their drought severity was categorized as severe ( $n = 13$ ), moderate ( $n = 30$ ), slight-mild ( $n = 31$ ), and normal ( $n = 41$ ). Figure 5 displays the sum of all VTCI values recorded in 2010, which shows that D-009 through D-361 experienced both drought and flooding. During 2010, D-009 to D-361 present the complete structure of drought and flood intensity and lasting flood spells presented in Figure 5. This indicates that the farming practices over the plain are irrigated and rainfed and categorized as mostly normal for winter crops. This demonstrates the better practices of VTCI monitoring in both rainfed and irrigated lands had very promising results.

#### 4.3. Determination of Flood Using GFMS Model

In Asia, the monsoon rain reaches the foothills of the Tibetan Plateau in early July to late July (JD 180–200) and withdraws in early September (around JD250) [28,60]. In this study, a flash flood occurred due to heavy monsoon rains in 2010, resulting in flood events in the period JD-200 to JD-232 (see Figure 6). The flood crashed down from the Himalayan mountain ranges (called ‘The Third Pole’ of the world) located in the north of Pakistan [61]. The plain of Punjab is located in the Indus basin, which contains five rivers. And the five rivers of Punjab mainly flooded during the summer of 2010 (monsoon) due to heavy rainfall and snow melt of the Himalaya mountain range in the north of Pakistan [62]. From the north of Pakistan, the flood streams flow into the Arabian Sea located in the south of the country. Due to this, the area is prone to drought and flooding.

The GFMS model was used for the validation of the VTCI approach results in terms of flood detection and intensity in 2010. The GFMS model was evaluated for its performance and accuracy in flood detection against flood events. This utilizes the real-time TRMM rainfall-incorporated data product and the TMPA precipitation data product obtained from the NASA Goddard TRMM/GPM Precipitation Processing System (PPS) [52,63]. TRMM (NASA and the Japan Aerospace Exploration (JAXA) Agency joint mission) contributed a 17-year (November 1997 to April 2015) dataset of global precipitation and lightning for measuring rainfall events, floods, drought, and weather forecasting [64–66]. The flood stream flow and detection/intensity at the specified stations incorporated the quasi-global hydrological real-time-based calculations at  $1/8^{\text{th}}$  degree for the measured water depth (mm) above the flood threshold with temporal resolution [59]. The GFMS model

determines the streamflow above the flood threshold at 1 km, flood stream flow at 12 km, flood detection/intensity at 1 km, and the hourly precipitation plot at 1 km resolution, respectively, in the stations/region.

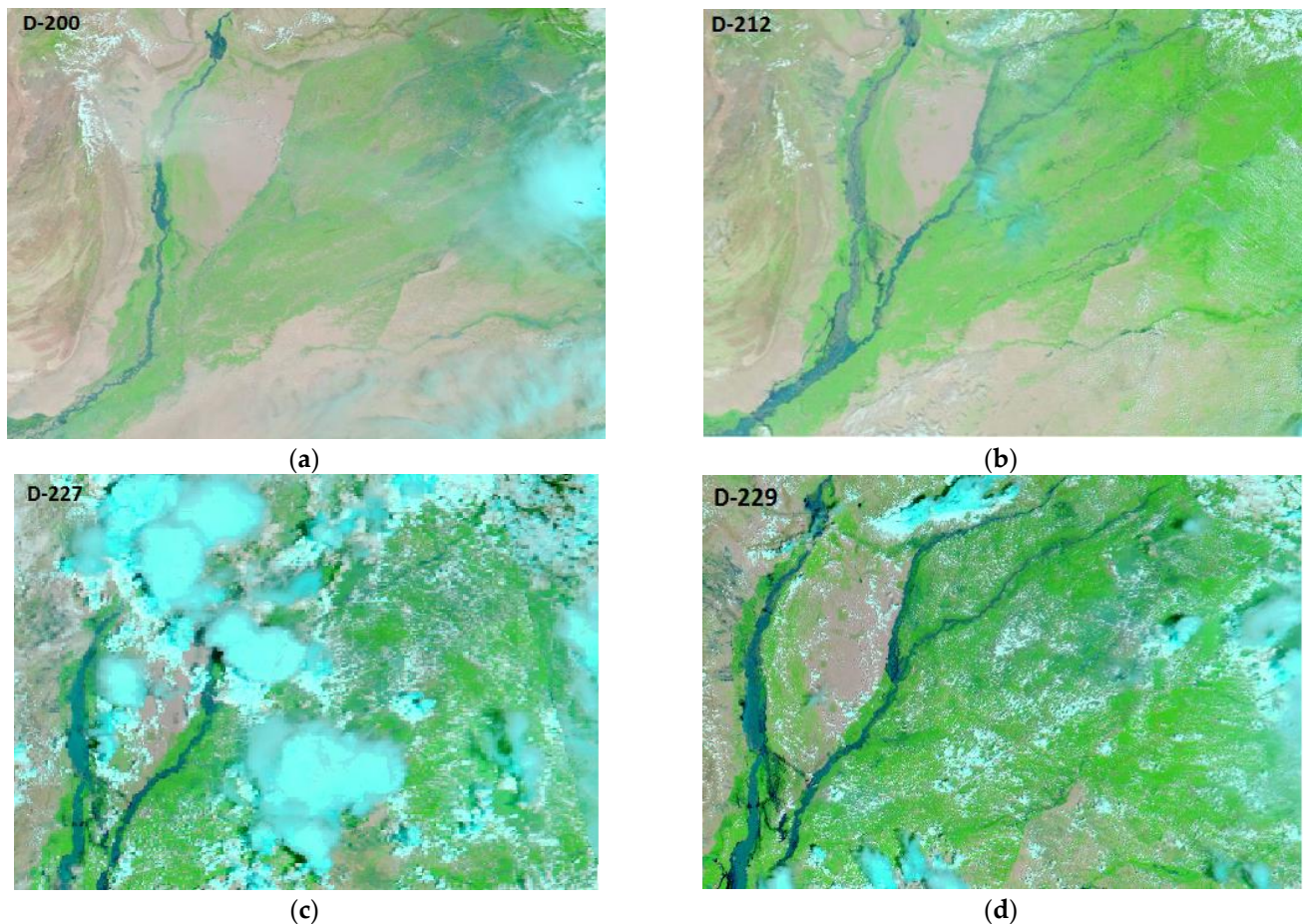


**Figure 6.** MODIS imagery of the flash flood from monsoon rains during 2010 at (a) JD-200, (b) JD-212, and (c) continuing at JD-227 as well as (d) at JD-229. The flowed down rapidly from the Himalayan mountain ranges (northern Pakistan) and muddy water swept over the southern plain of Punjab.

The defined GFMS model was considered in a one-year (2010) retrospective manner against the region and flow observations from five stations gauge stream as well as flood events and precipitation from north to south over the plain of Punjab, Pakistan. The sound, validated model-based Global Flood Archive (GFA) will be very helpful in evaluating variation and change of flood and intense precipitation across various spatial-temporal scales.

The GFMS model identifies the flood events in the period JD 201-232 and shows very decisive and promising results. Therefore, the GFMS model calculations are in good agreement with our results for the year 2010 utilizing the MODIS VTCI's 16-day acquired and mapped imagery.

Moreover, the streamflow above the flood threshold moved over to the south of the plain through the Indus basin, as observed by the five stations of the plain. Hence, flooding in the main Indus River of the plain passed from the northeast and northwest as well as from the southwest (the contiguous area of the Indian-Punjab) and continued through the south of the plain (i.e., MLN 1 and MLN 2), which showed a stream flow above the threshold at 1 km resolution. The flood events presented at MLN 1 and MLN 2 located in Multan (in south of the region) are shown in Figure 7c,e, and those for FSD 1 and FSD 2 located in Faisalabad (in the center of the plain) are presented in Figure 7a,d. The flood events for LHR at Lahore (in the northeast of the plain) are presented in Figure 7b.

These data describe the flood time, duration, and intensity at five weather stations. In contrast, the flood stream flows at 12 km resolution in the region are presented in Figure 8 for the JD (201–281) period during 2010. In general, the flood events return to normality in JD 249 in the broad picture when considering all calculations.

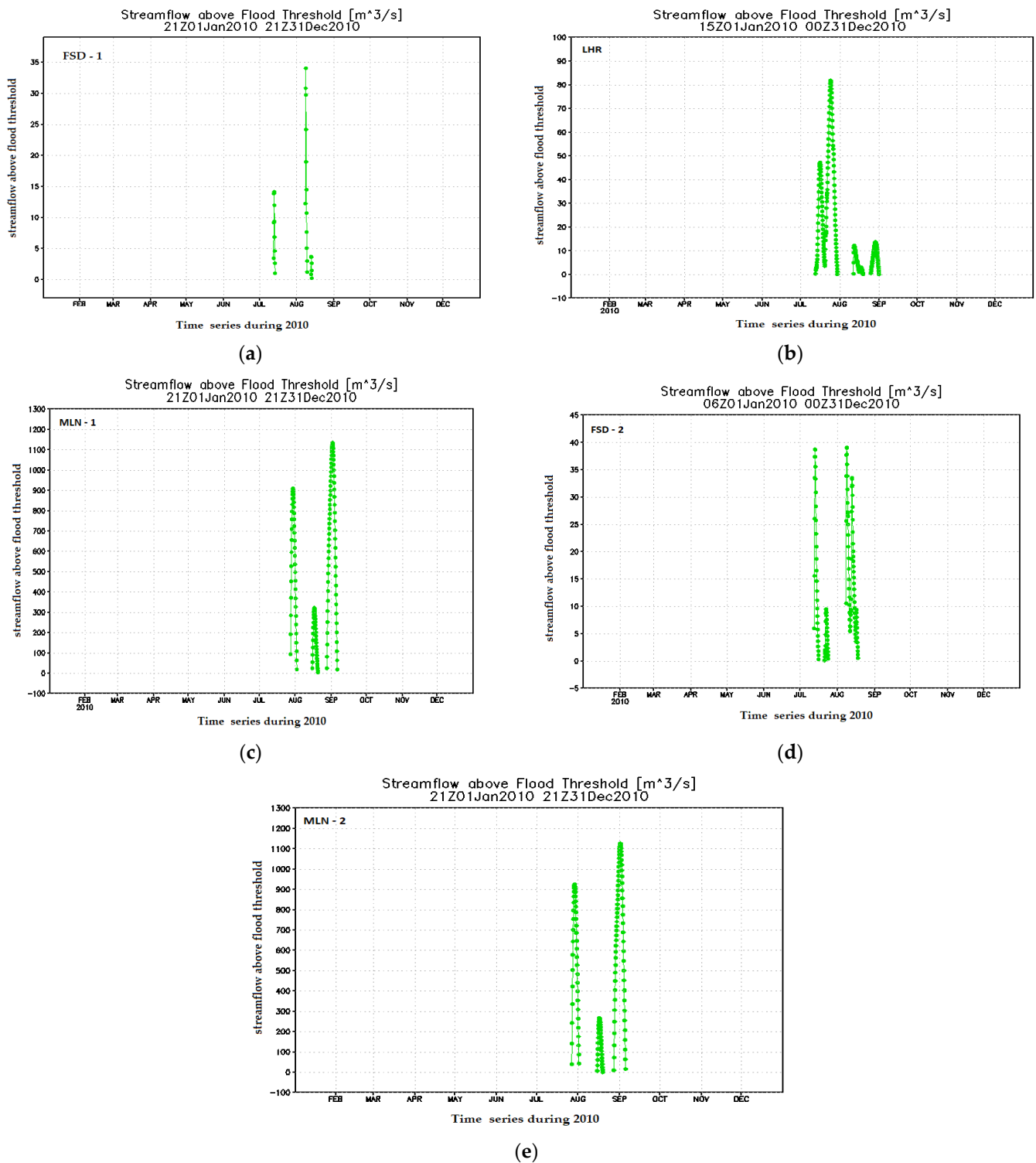
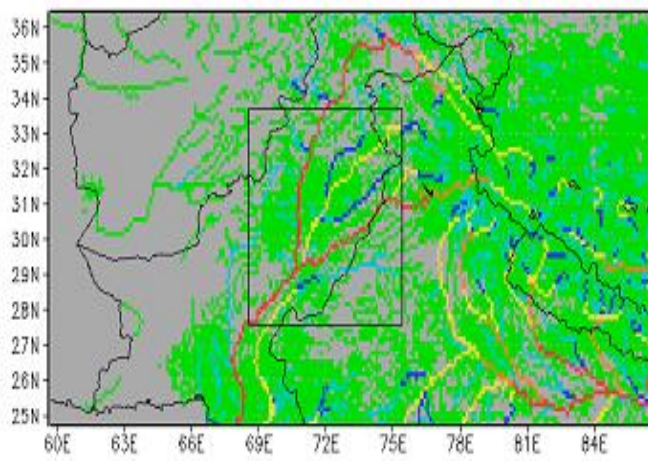
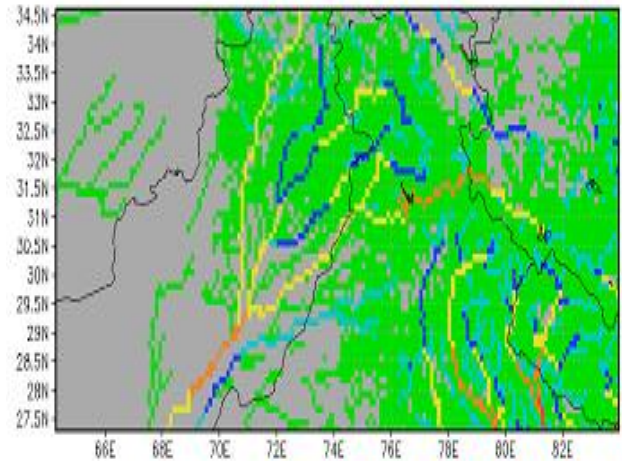


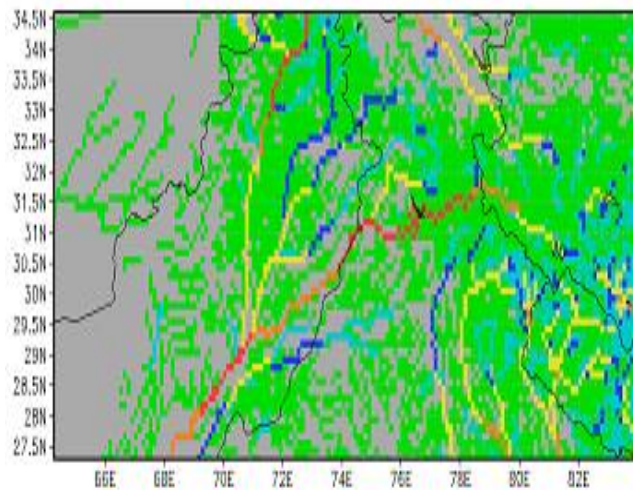
**Figure 7.** The monthly flood streamflow (above flood threshold) events time series at 3 h intervals over five weather stations (21Z01Jan2010 to 21Z31Dec2010): (a) FSD 1, (d) 2 FSD stations located in the south, (b) LHR located in the northeast, (c) MLN 1 in the center of the plain, and (e) MLN 2, also located in the center of the plain.



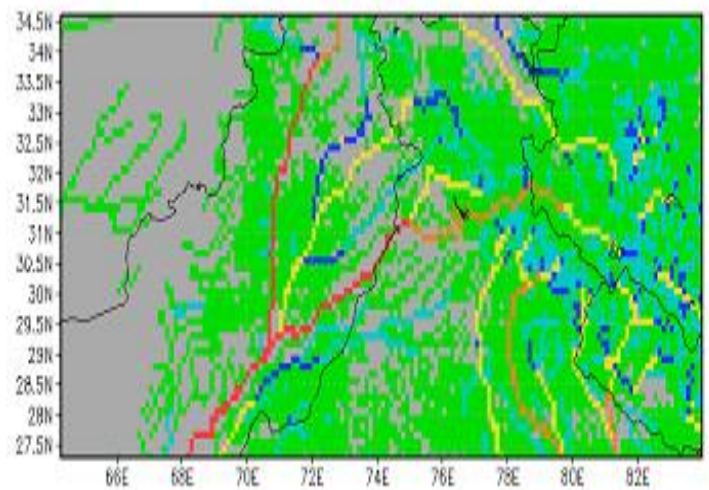
(a)



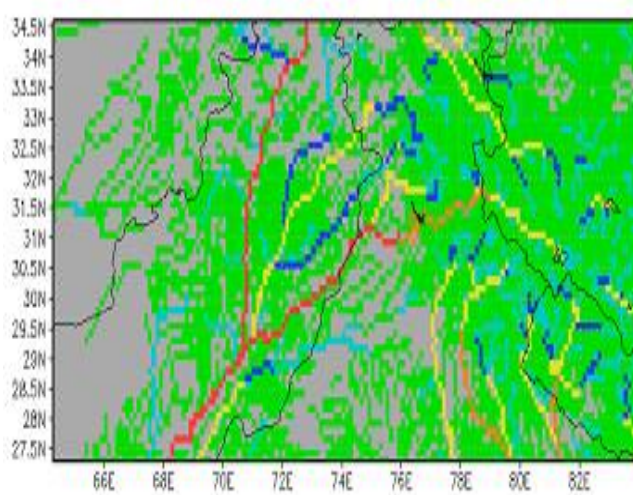
(b)



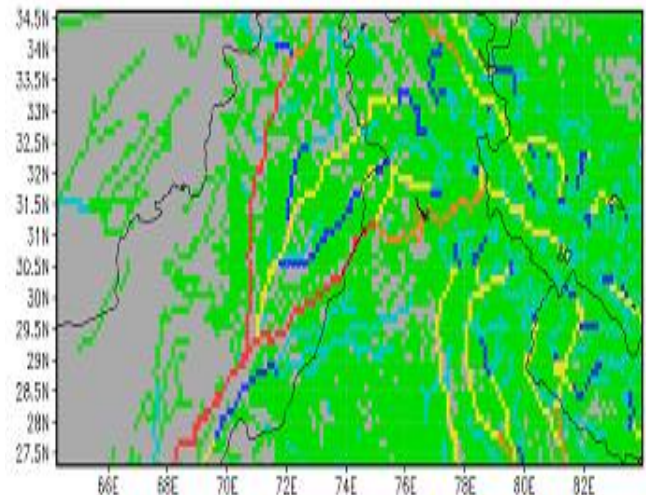
(c)



(d)



(e)



(f)

Figure 8. Cont.

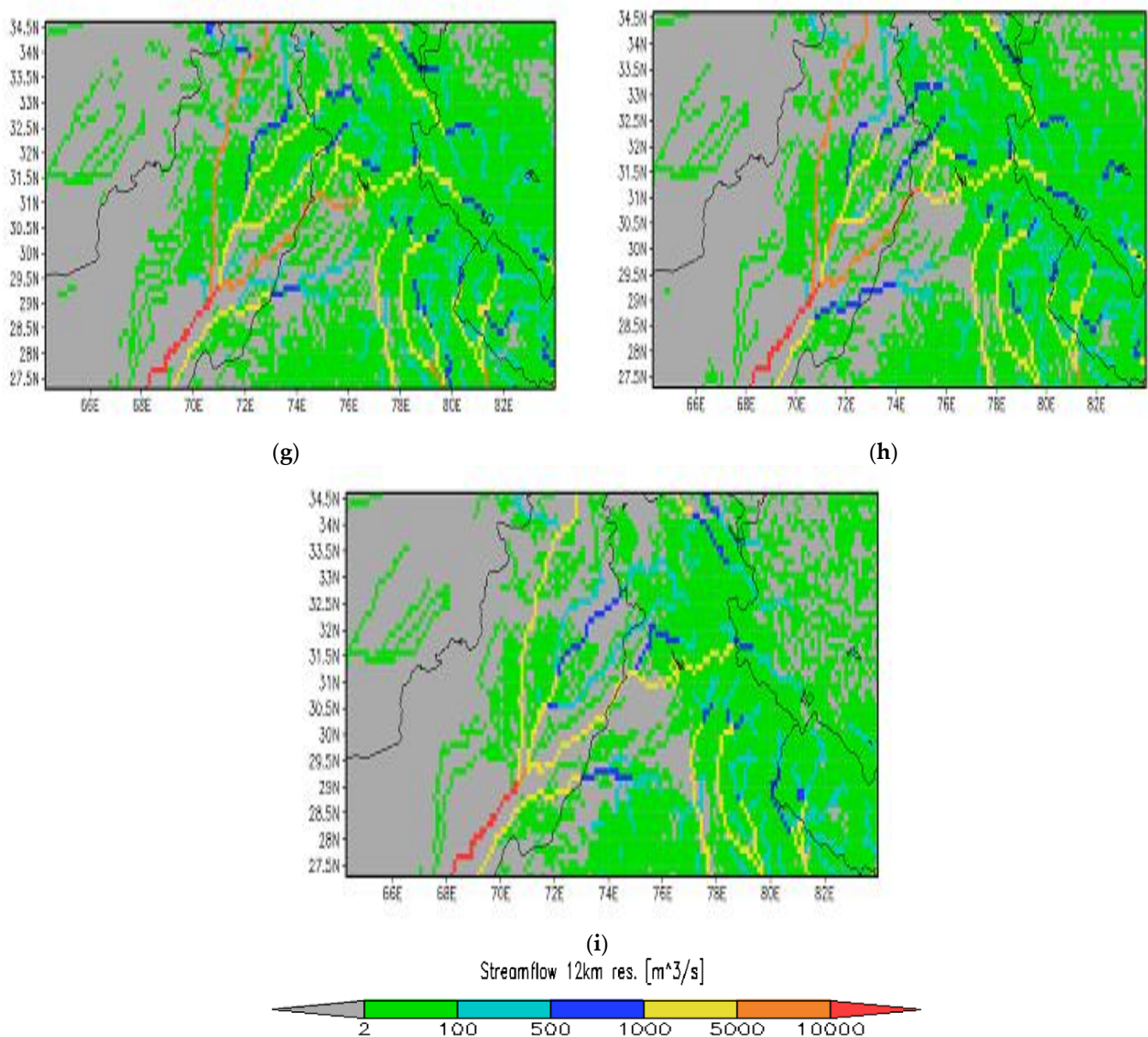


**Figure 8.** The streamflow events with temporal resolution (3 h interval) at relatively high spatial resolution (~12 km) over the region. (b–i) highlight the flood stream flow for the time series 21Z20July2010 to 21Z08Oct2010, which shows a maximum water flow above the threshold and ending in the south of the region as the plain returns to normal conditions. Water flows are also shown for the Indus basin that are categorized as normal for winter wheat crop seasons during 2011–2014. In contrast, (b–i) show the flood streamflow events that occurred on 20 July, 29 July, 2 August, 9 August, 13 August, 26 August, 31 August and 8 October, 2010, respectively, and (a) presents the flood stream flow and legends streamflow of over the entire country.

Figure 9 shows the flood detection and intensity (depth above threshold) with a ~1 km pixel area over the selected region and demonstrates that the Indus River and four shallow rivers contribute in the form of flood events. This also presents the plain in terms of wetlands due to extreme moisture contents in the JD 201–232 period during 2010. Figure 9a demonstrates the complete construction of flood events and spells over the region. Figure 9b presents the first spell of the flood, and Figure 9c–i illustrate the flood spells in the region. Subsequently, Figure 8d–f show the severe intensity of flood events from north to south of the plain. They show flood intensity and high peaks that are above the threshold in the

south of the region compared with the north and central area of the plain. Figure 9h,i show the flood events and runoff of flood events.

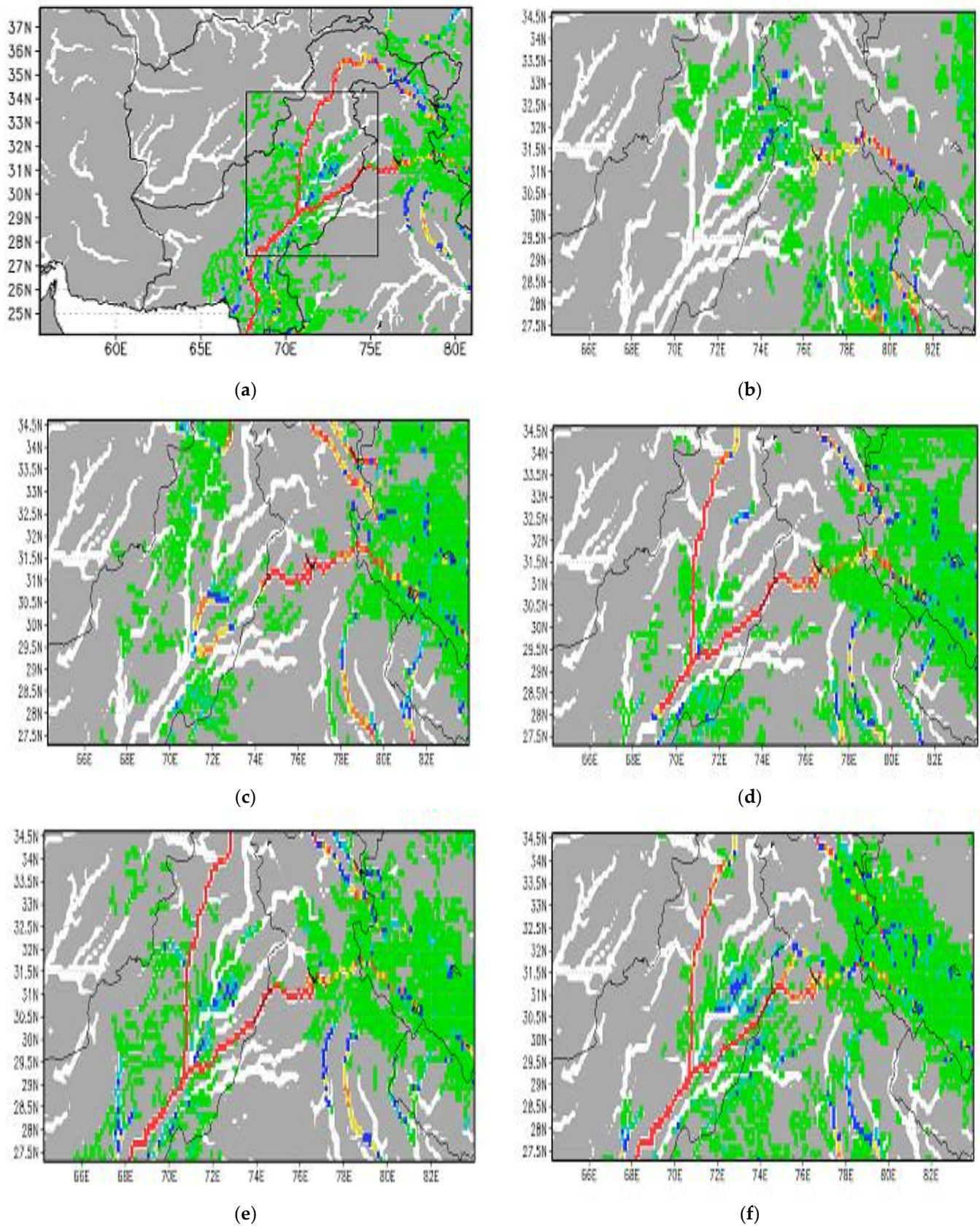
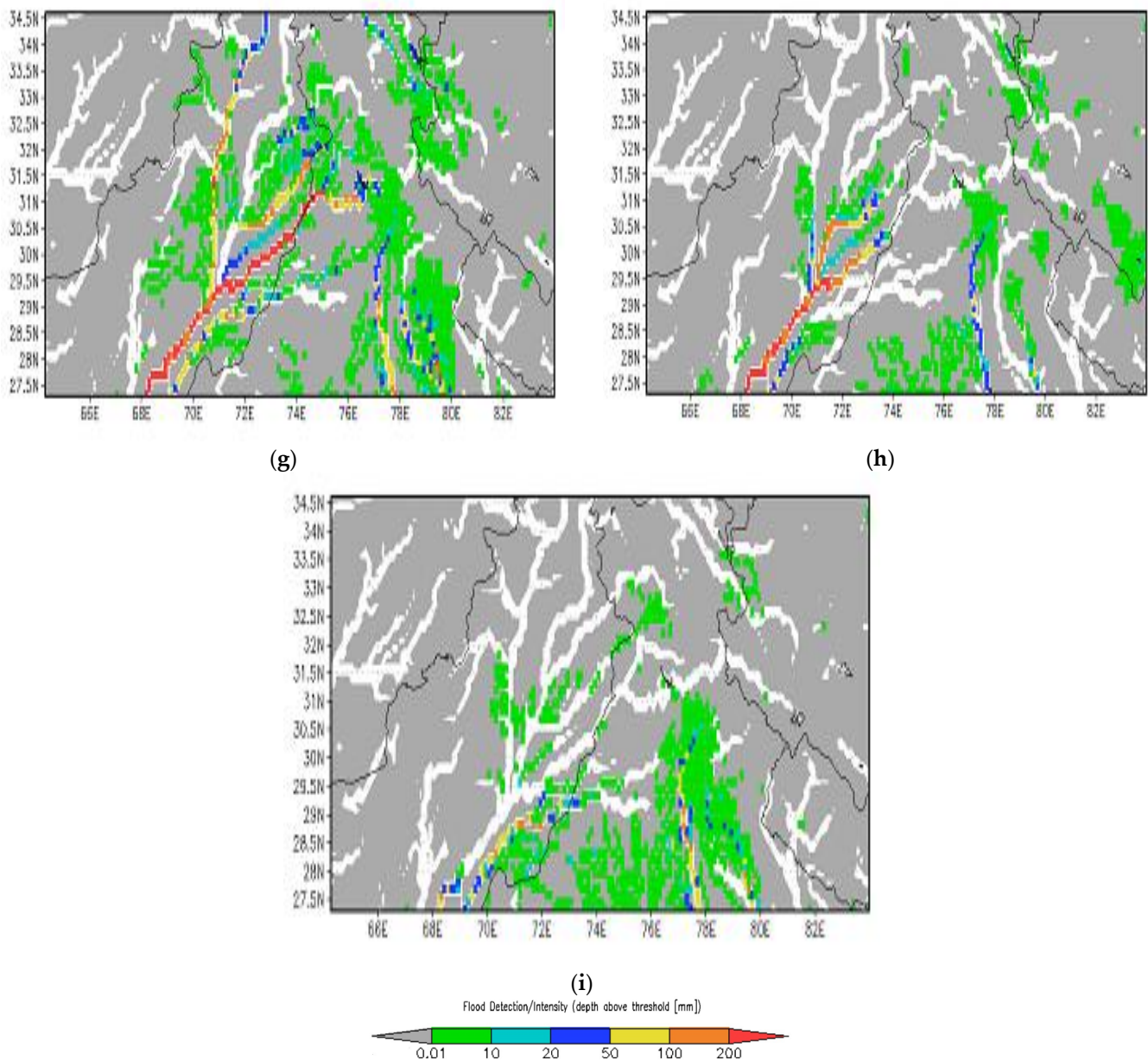


Figure 9. Cont.

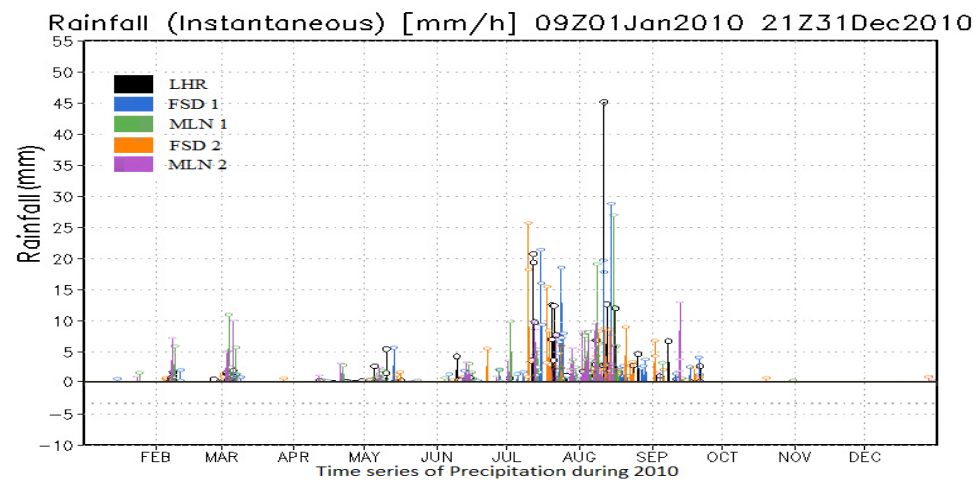


**Figure 9.** Flood detection/intensity above the flood threshold from 21Z20July2010 to 21Z06Sep2010 with water depth in (mm) at 1 km pixel area resolution. This depicts the maximum flood intensity above the threshold in the region and the normal conditions for winter season during 2010. (b–i) show the flood streamflow events that occurred on 20 July, 29 July, 2 August, 9 August, 13 August, 26 August, 31 August and 8 October, 2010, respectively, and (a) presents the flood detection/intensity and legends of intensity over the entire country.

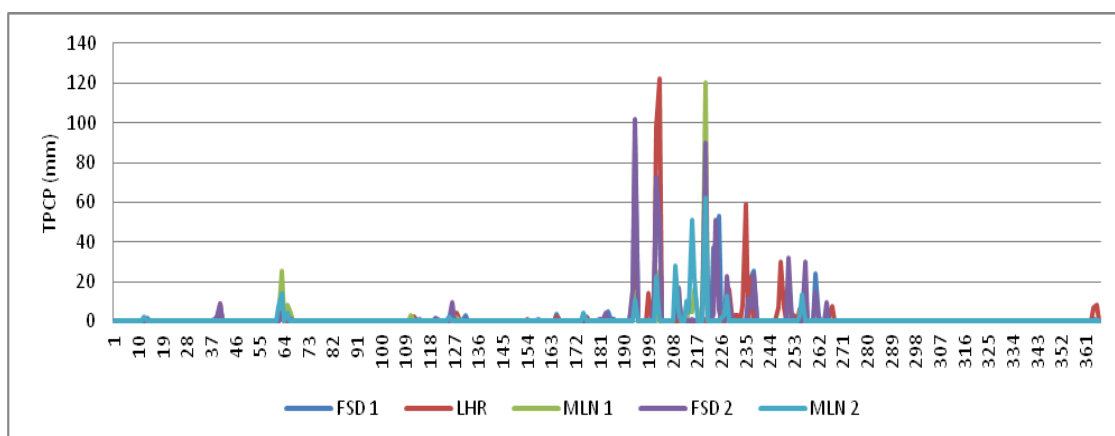
It was noted that the streamflow duration at 12 km resolution is due to the flood event on 8 October 2010, whereas, at 1 km resolution, the flood detection/intensity is due to the 8 September 2010 event. This shows that the area has good conditions for winter-wheat-crop farming.

Figure 10 shows that the TRMM and TMPA satellites archives of hourly real-time data are in good agreement with the PMD daily/monthly accumulative precipitation data presented in Figure 11. This could be validated with VTCI imagery over five weather stations (i.e., the relationship of VTCI values and ground-measured daily precipitation data presented in Tables 2 and 3). The observed results of the GFMS model events in the inundation plot time series (21Z01Jan2010 to 21Z31Dec2010) on each of five stations for

flood streamflow at 1 km and 12 km resolution and flood intensity at 1 km resolution as well as the hourly precipitation plot at 1 km resolution show the flood events during 2010.



**Figure 10.** Real-time TRMM and TMPA rainfall data with temporal resolution. Real-time rainfall (instantaneous mm/h) data at 1 km resolution during (09Z01Jan2010 to 21Z31Dec2010) for five stations show heavy rainfall from JD-185 to JD-232.



**Figure 11.** Pakistan Meteorology TPCP at (~1 km) spatial data (near-real-time daily rainfall accumulative data in mm) are accumulated for one month over five stations and show heavy rainfall from JD-185 to JD-232.

Our results for the GFMS model reveal that flood detection in the JD 201–232 period was very decisive and promising. The VTCI imagery and daily accumulative precipitation with collateral information are in good agreement with the high accuracy determinations of flood detection with the GFMS model using real-time TMPA anomalies over the five weather stations and over the region.

For the 2010 flood events, the flood time, duration, and intensity determined utilizing the MODIS VTCI imagery along with the daily measured precipitation for the validation of flood in the time series of 2010 over Punjab's plain were in good agreement with GFMS statistics. This shows that the GFMS model using real-time TRMM flood events is in considerable agreement with accurate determinations in the region. In general, the determined flood detection and intensity using the GFMS model that utilized the Goddard TRMM/GPM data products for flood event detection against flood event archives in time series plots results, validate our VTCI approach for flood detection and intensity in 2010 and are very promising for our determined and validated MODIS VTCI results presented in Figure 5 and Table 2.

**Table 2.** The linear correlation coefficients between VTCI imagery from D-009 to D-361 during 2010 and cumulative precipitation anomalies for the 16-day to 12-month periods during 2009–2010.

TPCP/VTCI	16-Days	1-	2-	3-	4-	5-	6-	9-	12-Months
D-009	−0.2370	−0.2370	−0.2370	0.1902	0.7360	0.7494	0.9484	0.9426	0.9364
D-025	0.7707	0.6731	0.6731	0.7055	0.7160	0.3573	0.4164	0.5456	0.5881
D-041	0.5552	0.8509	0.8130	0.8130	0.7930	0.8174	0.8822	0.8706	0.8407
D-057	0.6663	0.6663	0.7374	0.7374	0.7292	0.7298	0.3822	−0.2044	−0.2223
D-073	-	−0.6777	−0.5691	−0.6163	−0.6163	−0.6083	−0.3467	0.9356	0.9562
D-089	-	-	−0.5707	−0.5058	−0.5058	−0.4871	−0.3691	0.8096	0.8024
D-105	0.0579	0.0579	−0.0395	0.0494	0.0759	0.0759	0.0544	0.2428	0.2017
D-121	0.6399	0.7453	0.7453	−0.5590	−0.3661	−0.3661	−0.3502	0.8882	0.9767
D-137	−0.3942	0.6505	0.6618	−0.2967	−0.0898	−0.0878	−0.0878	0.9864	0.7055
D-153	0.4068	0.3925	0.5992	0.5992	−0.1453	0.0662	0.0662	0.9440	0.5541
D-169	−0.2972	−0.3412	−0.3553	−0.2760	0.9380	0.8019	0.9748	0.6764	−0.1636
D-185	−0.2373	−0.2278	−0.2233	−0.2667	−0.2667	−0.4596	−0.4078	−0.3914	−0.2077
D-217	−0.9365	−0.5398	−0.5350	−0.5330	−0.5498	−0.5498	−0.6216	−0.6026	−0.5628
D-233	0.8031	0.8321	0.9555	0.9554	0.9555	0.9577	0.9554	0.9544	0.9046
D-249	0.3012	0.2084	0.3447	0.4074	0.4109	0.4282	0.4282	0.4531	0.4791
D-265	0.1182	0.5447	0.8226	0.7347	0.7442	0.7444	0.7460	0.7490	0.7525
D-281	0.3447	0.7210	0.8607	0.9637	0.9723	0.9743	0.9770	0.9766	0.9741
D-297	−0.4590	−0.1984	0.6688	0.8888	0.8922	0.8973	0.8979	0.9000	0.8994
D-313	-	−0.4774	0.7258	0.8912	0.8997	0.8910	0.8953	0.8921	0.8920
D-329	-	-	0.4081	0.5479	0.5629	0.7039	0.7076	0.7027	0.7024
D-345	-	-	−0.2688	0.7983	0.9026	0.8481	0.8255	0.8347	0.8356
D-361	0.0569	0.0569	0.0569	0.0459	0.6350	0.8031	0.7483	0.7382	0.7346

**Table 3.** The linear correlation coefficient between VTCI imagery values from D-009 to D-169 during 2011–2014 for the 16-day to the 12-month periods during 2010–2014.

TPCP/VTCI	16-Days	1-	2-	3-	4-	5-	6-	9-	12-Months
009	0.5308	0.4341	0.3376	0.3006	0.1419	0.4322	0.224	0.3223	0.2657
025	−0.2478	−0.0902	0.0476	0.0559	0.0909	0.4411	0.6262	0.6128	0.588
041	0.3079	−0.1691	−0.0202	−0.0688	−0.0635	−0.0288	0.321	0.7714	0.7694
057	0.2208	−0.195	−0.4106	−0.3219	−0.3137	−0.3056	−0.1252	0.367	0.3696
073	0.2334	0.2127	−0.0754	−0.0949	−0.0672	−0.0526	−0.0525	0.1128	0.1392
089	0.345	0.264	0.4045	0.1507	0.2529	0.2539	0.2702	0.5461	0.5195
105	0.3296	0.3675	−0.1257	−0.1394	−0.0626	0.1661	−0.0048	0.1661	0.2983
121	0.1713	0.4424	0.1375	0.0969	−0.2438	−0.2513	−0.2476	0.0647	0.2345
137	0.5405	0.7249	0.7668	0.7139	0.4085	0.5091	0.4717	0.2003	0.6073
153	0.7177	0.7302	0.6985	0.6019	0.7072	0.6009	0.6209	0.5902	0.5489
169	0.2930	0.2738	0.2197	0.2374	0.158	0.1063	0.1726	0.1785	0.3951

For the 2010 flood events, we determined the flood time, duration, and intensity utilizing the MODIS, TRMM, and TMPA satellite data products. The near-real-time VTCI, TRMM, and TMPA observation and time series values are considered to be in agreement and to be of high accuracy in the determination of flood events in the region. In general, the determined flood detection and intensity as well as streamflow runoff above the flood threshold that utilized the Goddard TRMM/GPM data products for flood events detection against flood validate the VTCI monitoring approach for dry and wet conditions. Largely, the utilized MODIS, TRMM, and TMPA data products illustrate the flood events in the region vigorously and revolve around significant and insignificant drought and flood conditions with all calculations for the 2011–2014 crop seasons.

#### 4.4. Validation of Flood and Drought

We investigated the drought and flood over the region and found that there was no slight-mild drought, moderate or severe drought conditions during the period 2011–2014,

and normality was present at D-041, as shown in Figure 4. For the D-009 to D-361 period during 2010, the drought is categorized with certain fractional values from 0.28 to 1.0 (i.e., severe drought to wetness), as presented in Figure 5. Figure 5 shows the spatial variability of the flood (duration, time, and intensity) caused by the heavy rainfall in the period JD 185–232, and this generalizes the characteristics of SM and flood events in JD 201–232 during the year 2010. These show that normalcy has returned to the central plain, and farming is profitable from the south to the north during the winter.

For the validation of flood and drought, we consider the daily precipitation values at five stations geospatially along with VTCI imagery values in given periods over the plain of Punjab. In addition, the daily precipitation was used for the validation of VTCI imagery in the D-009 to 361 period during 2010 with TPCP (16-days to 12-month periods) during 2009–2010 to analyze the time, duration, and intensity of floods (Table 2). During 2010, the relationship between VTCI imagery and precipitation anomalies at D-201 was established as non-linear, and at D-217, a negative correlation was observed, which indicates the time, duration, and intensity of flood during 2010 (i.e., soil wetness was categorized as ‘1.0’ on the fractional scale of VTCI as the water levels gradually increased due to heavy rainfall, as shown in Figure 5 and Table 2). However, at D-281, a significant correlation ( $r = 0.95$ ) was noted, which clearly shows the return of normal condition on the plain (Table 2). These findings indicate the monsoon’s heavy rain and flood during summer do not affect the winter crop in the following year.

The VTCI values at D-041 ( $r = 0.77$ ,  $p < 0.005$ ) had the strongest linear connection with the TPCP throughout the nine-month study period (i.e., the relationship of the VTCI drought in the first 16 days of February during 2011–2014 with 9-month accumulative precipitation from 2010–2014). At D-041, a significant relationship was also observed with the 12-month TPCP anomaly period shown in Table 3 and Figure 12, while D-153 (May first, 16 days) had a significant correlation with the precipitation anomaly in early summer, showing the normal condition of weather in the region (see Table 3).

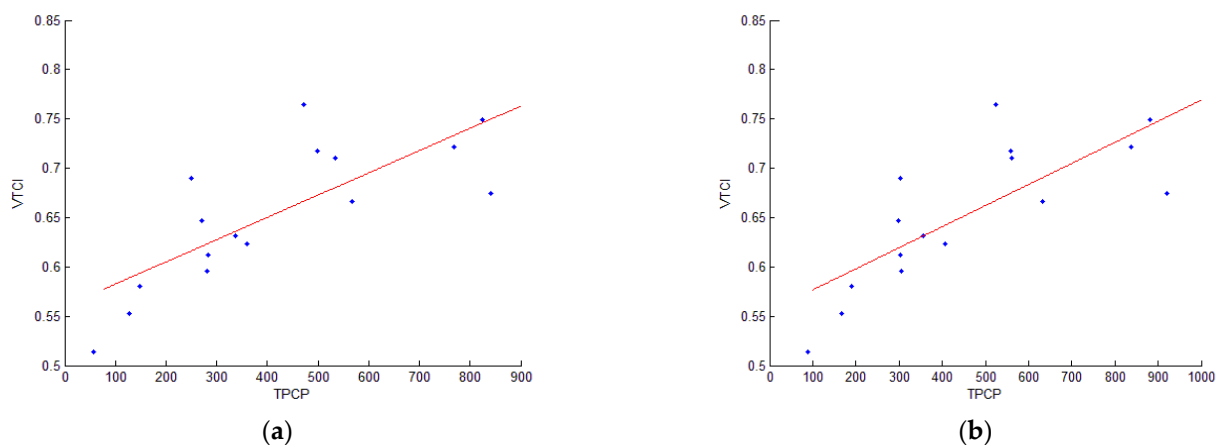


**Figure 12.** The linear correlation coefficient of the VTCI imagery values at D-041 during 2011–2014 and the TPCP anomaly at (a) D-288 and (b) D-384 during 2010–2014 at five stations.

There are five rivers (Indus River, Sutlej, Ravi, Beas, and Chenab) passing through the plain of Punjab. Punjab’s plain is both rainfed and irrigated, while the northeastern farms are primarily rainfed for unknown reasons [64,65]. When VTCI images are combined with daily precipitation data, a clear picture of precipitation anomalies may be highlighted. Our findings show that most of the southern farms received below than average precipitation compared with the northern areas. This shows that the plain is irrigated as well as rainfed, and also that the impact of heavy rainfall causes unprecedented damage to crops and the land of Punjab. Generally, the southern region of the plain with low precipitation has low VTCI values, while adequate precipitation in the northeast region results in high

VTCI values. This shows that the region does not only depend on irrigated practices but precipitation anomalies.

Furthermore, it was noticed that the VTCI imagery had a very significant relationship with the TPCP. This demonstrates that the VTCI imagery is related to recent precipitation but also correlates to past precipitation during the winter wheat crop season, as shown in Tables 2 and 3 and Figure 12.

Regarding the VTCI imagery from D-009 to D-361 during 2010, the TPCP anomaly periods from (16-days, 1, 2, 3, 4, 5, 6, 9, and 12-month) to (16, 32, 64, 96, 128, 160, 288, and 384-days) was set during 2009–2010 (i.e., the VTCI 16 day-imagery corresponds to 16-day TPCP and is counted as multiples from 1 to 12 months). Hence, D-201 was established as nonlinear during 2010 due to flood events; therefore, the values are not presented here, whereas (-) represents a 'non' value in the given time and periods. The VTCI values, therefore, relate to both recent and historical TPCP anomalies.

Moreover, it was determined that the connection between the VTCI and TPCP anomaly varies with season and time as well as the region. Overall, the relationship was positive in the winter crop seasons during 2011–2014. Similarly, during the 2010 winter and early summer in D-009 to D-153, the relationship was significant. This indicates that VTCI and TPCP have a positive association during the winter and early summer. The MODIS VTCI imagery in particular, gives an improved map of all places from D-009 to D-169 for drought during 2011–2014 and from D-009 to D-361 during 2010 for drought and flood occurrences (flood time, length, and severity) over the plain of Punjab. This work reveals broad agreement with Wan et al. [20] who analyzed the southern Great Plain of the United States and Sun et al. [21] who analyzed a VTCI time-series based in China's Guanzhong plain regarding drought monitoring and warm and cold borders.

In addition, the considered GFMS model for the evaluation of inundation plot time series on each of the five stations/regions during the 2010 flood stream flow above the threshold, flood stream flow at high spatial (~12 km) resolution, and flood detection/intensity as well as hourly precipitation plot at ~1 km resolution demonstrates the flood detection/intensity in the JD 185–232 period and shows a very clear and promising result.

Finally, based on our investigation of droughts and the record-breaking flood in late July to early September 2010 which affected the region in the period D-201 to D-217, the region was categorized as principally normal for the period D-233 to D-361 during 2010 and for 4 years (2011–2014), and overall, for the five years of winter wheat-crop seasons during the period (2010–2014). The analysis of the vegetation and temperature-related drought indices demonstrates that the results obtained from the VTCI approach are in good agreement across the plain of Punjab. The investigation of drought during 2011–2014 and flood in 2010, which severely affected the region in the JD 185–232 period, was categorized the region as normal for the years 2011–2014. The results show that the determination and validation of remotely-sensed data along with measured precipitation TPCP data during the time series of VTCI are in good agreement and do not affect the winter crop in the land of Punjab, Pakistan.

## 5. Conclusions

In this study, we quantify the VTCI index and characterize the drought levels using remote-sensing data, which reflects the agricultural and hydrological impacts over the region. The VTCI drought monitoring approach indicates the sensitivity of WACE in terms of SM and drought determination as well as flood (time, duration, and intensity) over the region. Despite the extreme weather and flood events in the region during 2010, the time-based changes of the land surface SM conditions could be categorized for 4 years (2011–2014). Over the five weather stations (located in north, central, and south of the region), the VTCI values (~n = 200) observed in the plain from severe to wet conditions during 2011–2014 ranged from 0.283 to 1.0. A total of 220 VTCI values were analyzed in the aforementioned occurrences, and their drought severity was classified as severe (n = 11), moderate (n = 18), slight-mild (n = 79), or normal (n = 112). For the identification of drought,

WACE suggests that the VTCI can detect moisture, drought, and flood in agricultural land during the 2010 seasons and 2011–2014 winter wheat crop growing seasons subjected to wet conditions and severe drought in the present study. The analysis of the single and multiyear WACE in the years 2011–2014 indicates that the 2010 flood events were considered normal in the following years and provided good conditions in the winter wheat crop seasons. This represents substantial normality for the 4-year period and response to seasonal change variations during the winter wheat crop season spanning 2011–2014. However, during the 2010 heavy rainfall and flood events (JD 185–332), the SM states were subjected to abnormality due to extreme wetness. Consequently, the retreat states of the WACE are steady and present substantial normality in the region in fall 2010 and during the winter wheat crop seasons across 2011–2014.

In addition, it was observed that the VTCI 16-day acquired imagery and daily precipitation in the 2010 results were in line with the GFMS model for the flood stream flow, detection/intensity, and hourly precipitation anomaly using multi-satellite data over the region. These findings showed the good sensitivity of the VTCI to precipitation and SM in agricultural lands. In general, these demonstrate the monsoon's heavy rain or flood events during summer do not affect the winter crop over the plain of Punjab, Pakistan. It shows that there was no impact of flood during the period 2011–2014 and over the whole five-year period 2010–2014.

It was concluded that the NDVI, LST, and VTCI are very reasonable for drought monitoring during the winter wheat crop season as well as for flood events. In addition, the VTCI is favorable for drought assessment and to determine and validate the flood events and also to determine the WACE over the region in given time/seasons. This shows an essential connection between the VTCI and TPCP anomalies for detecting the hydrological events of agricultural droughts and floods over Punjab. Generally, our results indicate the monsoon's heavy rain or flood during summer marginally affects the winter crop over the plain of Punjab, Pakistan.

**Author Contributions:** Conceptualization, J.K. and R.U.; methodology, R.U.; software, J.K.; validation, J.K., R.U. and I.U.; formal analysis, I.U.; investigation, R.U.; resources, J.K.; data curation, J.K.; writing—original draft preparation, R.U.; writing—review and editing, I.U.; visualization, R.U.; supervision, R.U.; project administration, F.K. and Y.L.; funding acquisition, F.K. and Y.L. All authors have read and agreed to the published version of the manuscript.

**Funding:** This work was supported in part by the National Research Foundation of Korea (NRF) grant 2022R1G1A1003531 and Institute of Information & communications Technology Planning & Evaluation (IITP) grant IITP-2022-2020-0-101741, RS-2022-00155885 funded by the Korea government (MSIT).

**Data Availability Statement:** Not applicable.

**Conflicts of Interest:** The authors declare no conflict of interest.

## References

1. Sorooshian, S.; AghaKouchak, A.; Arkin, P.; Eylander, J.; Foufoula-Georgiou, E.; Harmon, R.; Hendrickx, J.M.H.; Imam, B.; Kuligowski, R.; Skahill, B.; et al. Advancing the Remote Sensing of Precipitation. *Bull. Am. Meteorol. Soc.* **2011**, *92*, 1271–1272. [[CrossRef](#)]
2. Shahzaman, M.; Zhu, W.; Bilal, M.; Habtemicheal, B.; Mustafa, F.; Arshad, M.; Ullah, I.; Ishfaq, S.; Iqbal, R. Remote Sensing Indices for Spatial Monitoring of Agricultural Drought in South Asian Countries. *Remote Sens.* **2021**, *13*, 2059. [[CrossRef](#)]
3. Shahzaman, M.; Zhu, W.; Ullah, I.; Mustafa, F.; Bilal, M.; Ishfaq, S.; Nisar, S.; Arshad, M.; Iqbal, R.; Aslam, R.W. Comparison of Multi-Year Reanalysis, Models, and Satellite Remote Sensing Products for Agricultural Drought Monitoring over South Asian Countries. *Remote Sens.* **2021**, *13*, 3294. [[CrossRef](#)]
4. Tanaka, M.; Sugimura, T.; Tanaka, S.; Tamai, N. Flood–drought cycle of Tonle Sap and Mekong Delta area observed by DMSP-SSM/I. *Int. J. Remote Sens.* **2003**, *24*, 1487–1504. [[CrossRef](#)]
5. Jin, Y.-Q. A flooding index and its regional threshold value for monitoring floods in China from SSM/I data. *Int. J. Remote Sens.* **1999**, *20*, 1025–1030. [[CrossRef](#)]
6. Rahimi, S.; Gholami Sefidkouhi, M.A.; Raeini-Sarjaz, M.; Valipour, M. Estimation of actual evapotranspiration by using MODIS images (a case study: Tajan catchment). *Arch. Agron. Soil Sci.* **2015**, *61*, 695–709. [[CrossRef](#)]

7. Justice, C.O.; Vermote, E.; Townshend, J.R.G.; Defries, R.; Roy, D.P.; Hall, D.K.; Salomonson, V.V.; Privette, J.L.; Riggs, G.; Strahler, A.; et al. The Moderate Resolution Imaging Spectroradiometer (MODIS): Land remote sensing for global change research. *IEEE Trans. Geosci. Remote Sens.* **1998**, *36*, 1228–1249. [[CrossRef](#)]
8. Sajjad, M.M.; Wang, J.; Abbas, H.; Ullah, I.; Khan, R.; Ali, F. Impact of Climate and Land-Use Change on Groundwater Resources, Study of Faisalabad District, Pakistan. *Atmosphere* **2022**, *13*, 1097. [[CrossRef](#)]
9. Kogan, F.N. Application of vegetation index and brightness temperature for drought detection. *Adv. Space Res.* **1995**, *15*, 91–100. [[CrossRef](#)]
10. Lu, E. Determining the start, duration, and strength of flood and drought with daily precipitation: Rationale. *Geophys. Res. Lett.* **2009**, *36*, L12707. [[CrossRef](#)]
11. Zargar, A.; Sadiq, R.; Naser, B.; Khan, F.I. A review of drought indices. *Environ. Rev.* **2011**, *19*, 333–349. [[CrossRef](#)]
12. Park, S.; Feddema, J.J.; Egbert, S.L. MODIS land surface temperature composite data and their relationships with climatic water budget factors in the central Great Plains. *Int. J. Remote Sens.* **2005**, *26*, 1127–1144. [[CrossRef](#)]
13. Liu, W.T.H.; Massambani, O.; Nobre, C.A. Satellite recorded vegetation response to drought in Brazil. *Int. J. Climatol.* **1994**, *14*, 343–354. [[CrossRef](#)]
14. AghaKouchak, A.; Farahmand, A.; Melton, F.S.; Teixeira, J.; Anderson, M.C.; Wardlaw, B.D.; Hain, C.R. Remote sensing of drought: Progress, challenges and opportunities. *Rev. Geophys.* **2015**, *53*, 452–480. [[CrossRef](#)]
15. Wilhite, D.A.; Glantz, M.H. Understanding: The Drought Phenomenon: The Role of Definitions. *Water Int.* **1985**, *10*, 111–120. [[CrossRef](#)]
16. Palmer, W.C. *Meteorological Drought*; U.S. Weather Bureau Research Paper No. 45; U.S. Department of Commerce, Weather Bureau: Silver Spring, MD, USA, 1965; Volume 58.
17. Byun, H.R.; Wilhite, D.A. Objective quantification of drought severity and duration. *J. Clim.* **1999**, *12*, 2747–2756. [[CrossRef](#)]
18. Dai, A. Drought under global warming: A review. *WIREs Clim. Chang.* **2011**, *2*, 45–65. [[CrossRef](#)]
19. Ullah, I.; Ma, X.; Yin, J.; Asfaw, T.; Azam, K.; Syed, S.; Liu, M.; Arshad, M.; Shahzaman, M. Evaluating the meteorological drought characteristics over Pakistan using in situ observations and reanalysis products. *Int. J. Climatol.* **2021**, *41*, 4437–4459. [[CrossRef](#)]
20. Ullah, I.; Ma, X.; Yin, J.; Saleem, F.; Syed, S.; Omer, A.; Habtemicheal, B.A.; Liu, M.; Arshad, M. Observed changes in seasonal drought characteristics and their possible potential drivers over Pakistan. *Int. J. Climatol.* **2022**, *42*, 1576–1596. [[CrossRef](#)]
21. Ali, M.; Ghaith, M.; Wagdy, A.; Helmi, A.M. Development of a New Multivariate Composite Drought Index for the Blue Nile River Basin. *Water* **2022**, *14*, 886. [[CrossRef](#)]
22. McKee, T.B.; Nolan, J.; Kleist, J. The relationship of drought frequency and duration to time scales. In Proceedings of the Eighth Conference on Applied Climatology, Anaheim, CA, USA, 17–22 January 1993.
23. Meng, L.; Shen, Y. On the Relationship of Soil Moisture and Extreme Temperatures in East China. *Earth Interact.* **2014**, *18*, 1–20. [[CrossRef](#)]
24. Wan, Z.; Wang, P.; Li, X. Using MODIS Land Surface Temperature and Normalized Difference Vegetation Index products for monitoring drought in the southern Great Plains, USA. *Int. J. Remote Sens.* **2004**, *25*, 61–72. [[CrossRef](#)]
25. Dai, A. Increasing drought under global warming in observations and models. *Nat. Clim. Chang.* **2013**, *3*, 52–58. [[CrossRef](#)]
26. Dai, A. Characteristics and trends in various forms of the Palmer Drought Severity Index during 1900–2008. *J. Geophys. Res. Atmos.* **2011**, *116*. [[CrossRef](#)]
27. Dai, A. Hydroclimatic trends during 1950–2018 over global land. *Clim. Dyn.* **2021**, *56*, 4027–4049. [[CrossRef](#)]
28. Zeng, X.; Lu, E. Globally Unified Monsoon Onset and Retreat Indexes. *J. Clim.* **2004**, *17*, 2241–2248. [[CrossRef](#)]
29. Findell, K.L.; Berg, A.; Gentile, P.; Krasting, J.P.; Lintner, B.R.; Malyshev, S.; Santanello, J.A.; Shevliakova, E. The impact of anthropogenic land use and land cover change on regional climate extremes. *Nat. Commun.* **2017**, *8*, 989. [[CrossRef](#)]
30. Ullah, I.; Ma, X.; Ren, G.; Yin, J.; Iyakaremye, V.; Syed, S.; Lu, K.; Xing, Y.; Singh, V.P. Recent Changes in Drought Events over South Asia and Their Possible Linkages with Climatic and Dynamic Factors. *Remote Sens.* **2022**, *14*, 3219. [[CrossRef](#)]
31. Ullah, I.; Ma, X.; Yin, J.; Omer, A.; Habtemicheal, B.A.; Saleem, F.; Iyakaremye, V.; Syed, S.; Arshad, M.; Liu, M. Spatiotemporal characteristics of meteorological drought variability and trends (1981–2020) over South Asia and the associated large-scale circulation patterns. *Clim. Dyn.* **2022**. [[CrossRef](#)]
32. Sun, W.; Wang, P.-X.; Zhang, S.-Y.; Zhu, D.-H.; Liu, J.-M.; Chen, J.-H.; Yang, H.-S. Using the vegetation temperature condition index for time series drought occurrence monitoring in the Guanzhong Plain, PR China. *Int. J. Remote Sens.* **2008**, *29*, 5133–5144. [[CrossRef](#)]
33. BAI, J.; YU, Y.; Di, L. Comparison between TVDI and CWSI for drought monitoring in the Guanzhong Plain, China. *J. Integr. Agric.* **2017**, *16*, 389–397. [[CrossRef](#)]
34. Gao, Z.; Wang, Q.; Cao, X.; Gao, W. The responses of vegetation water content (EWT) and assessment of drought monitoring along a coastal region using remote sensing. *GIScience Remote Sens.* **2014**, *51*, 1–16. [[CrossRef](#)]
35. Wang, L.; Qu, J.J. NMDI: A normalized multi-band drought index for monitoring soil and vegetation moisture with satellite remote sensing. *Geophys. Res. Lett.* **2007**, *34*, L20405. [[CrossRef](#)]
36. Peters, A.J.; Walter-Shea, E.A.; Ji, L.; Viña, A.; Hayes, M.; Svoboda, M.D. Drought monitoring with NDVI-based Standardized Vegetation Index. *Photogramm. Eng. Remote Sens.* **2002**, *68*, 71–75.
37. Parviz, L. Determination of effective indices in the drought monitoring through analysis of satellite images. *J. Agric. For.* **2016**, *62*, 305–324. [[CrossRef](#)]

38. Ma, X.; Yoshikane, T.; Hara, M.; Wakazuki, Y.; Takahashi, H.G.; Kimura, F. Hydrological response to future climate change in the Agano River basin, Japan. *Hydrol. Res. Lett.* **2010**, *4*, 25–29. [[CrossRef](#)]
39. Ma, X.; Fukushima, Y. A numerical model of the river freezing process and its application to the Lena River. *Hydrol. Process.* **2002**, *16*, 2131–2140. [[CrossRef](#)]
40. Zhou, H.; Zhou, W.; Liu, Y.; Yuan, Y.; Huang, J.; Liu, Y. Meteorological Drought Migration in the Poyang Lake Basin, China: Switching among Different Climate Modes. *J. Hydrometeorol.* **2020**, *21*, 415–431. [[CrossRef](#)]
41. Han, Y.; Wang, Y.; Zhao, Y. Estimating Soil Moisture Conditions of the Greater Changbai Mountains by Land Surface Temperature and NDVI. *IEEE Trans. Geosci. Remote Sens.* **2010**, *48*, 2509–2515. [[CrossRef](#)]
42. Goetz, S.J. Multi-sensor analysis of NDVI, surface temperature and biophysical variables at a mixed grassland site. *Int. J. Remote Sens.* **1997**, *18*, 71–94. [[CrossRef](#)]
43. Coll, C.; Hook, S.J.; Galve, J.M. Land Surface Temperature From the Advanced Along-Track Scanning Radiometer: Validation Over Inland Waters and Vegetated Surfaces. *IEEE Trans. Geosci. Remote Sens.* **2009**, *47*, 350–360. [[CrossRef](#)]
44. Adnan, S.; Ullah, K.; Shouting, G. Investigations into precipitation and drought climatologies in south central Asia with special focus on Pakistan over the period 1951–2010. *J. Clim.* **2016**, *29*, 6019–6035. [[CrossRef](#)]
45. Hina, S.; Saleem, F.; Arshad, A.; Hina, A.; Ullah, I. Droughts over Pakistan: Possible cycles, precursors and associated mechanisms. *Geomat. Nat. Hazards Risk* **2021**, *12*, 1638–1668. [[CrossRef](#)]
46. Sein, Z.M.M.; Ullah, I.; Iyakaremye, V.; Azam, K.; Ma, X.; Syed, S.; Zhi, X. Observed spatiotemporal changes in air temperature, dew point temperature and relative humidity over Myanmar during 2001–2019. *Meteorol. Atmos. Phys.* **2022**, *134*, 7. [[CrossRef](#)]
47. Sein, Z.M.M.; Zhi, X.; Ullah, I.; Azam, K.; Ngoma, H.; Saleem, F.; Xing, Y.; Iyakaremye, V.; Syed, S.; Hina, S.; et al. Recent variability of sub-seasonal monsoon precipitation and its potential drivers in Myanmar using in-situ observation during 1981–2020. *Int. J. Climatol.* **2022**, *42*, 3341–3359. [[CrossRef](#)]
48. Mie Sein, Z.M.; Ullah, I.; Saleem, F.; Zhi, X.; Syed, S.; Azam, K. Interdecadal Variability in Myanmar Rainfall in the Monsoon Season (May–October) Using Eigen Methods. *Water* **2021**, *13*, 729. [[CrossRef](#)]
49. Mie Sein, Z.; Ullah, I.; Syed, S.; Zhi, X.; Azam, K.; Rasool, G. Interannual Variability of Air Temperature over Myanmar: The Influence of ENSO and IOD. *Climate* **2021**, *9*, 35. [[CrossRef](#)]
50. Sheikh, M.M.; Manzoor, N.; Ashraf, J.; Adnan, M.; Collins, D.; Hameed, S.; Manton, M.J.; Ahmed, A.U.; Baidya, S.K.; Borgaonkar, H.P.; et al. Trends in extreme daily rainfall and temperature indices over South Asia. *Int. J. Climatol.* **2015**, *35*, 1625–1637. [[CrossRef](#)]
51. Ahmed, K.; Shahid, S.; Chung, E.S.; Wang, X.J.; Harun, S.B. Climate change uncertainties in seasonal drought severity-area-frequency curves: Case of arid region of Pakistan. *J. Hydrol.* **2019**, *570*, 473–485. [[CrossRef](#)]
52. Arshad, M.; Ma, X.; Yin, J.; Ullah, W.; Ali, G.; Ullah, S.; Liu, M.; Shahzaman, M.; Ullah, I. Evaluation of GPM-IMERG and TRMM-3B42 precipitation products over Pakistan. *Atmos. Res.* **2021**, *249*, 105341. [[CrossRef](#)]
53. Arshad, M.; Ma, X.; Yin, J.; Ullah, W.; Liu, M.; Ullah, I. Performance evaluation of ERA-5, JRA-55, MERRA-2, and CFS-2 reanalysis datasets, over diverse climate regions of Pakistan. *Weather Clim. Extrem.* **2021**, *33*, 100373. [[CrossRef](#)]
54. Xing, Y.; Shao, D.; Liang, Q.; Chen, H.; Ma, X.; Ullah, I. Investigation of the drainage loss effects with a street view based drainage calculation method in hydrodynamic modelling of pluvial floods in urbanized area. *J. Hydrol.* **2022**, *605*, 127365. [[CrossRef](#)]
55. Liu, M.; Ma, X.; Yin, Y.; Zhang, Z.; Yin, J.; Ullah, I.; Arshad, M. Non-stationary frequency analysis of extreme streamflow disturbance in a typical ecological function reserve of China under a changing climate. *Ecohydrology* **2021**, *23*, e2323. [[CrossRef](#)]
56. Iyakaremye, V.; Zeng, G.; Yang, X.; Zhang, G.; Ullah, I.; Gahigi, A.; Vuguziga, F.; Asfaw, T.; Ayugi, B. Increased high-temperature extremes and associated population exposure in Africa by the mid-21st century. *Sci. Total Environ.* **2021**, *790*, 148162. [[CrossRef](#)]
57. Uwimbabazi, J.; Jing, Y.; Iyakaremye, V.; Ullah, I.; Ayugi, B. Observed Changes in Meteorological Drought Events during 1981–2020 over Rwanda, East Africa. *Sustainability* **2022**, *14*, 1519. [[CrossRef](#)]
58. Tian, M.; Wang, P.; Khan, J. Drought Forecasting with Vegetation Temperature Condition Index Using ARIMA Models in the Guanzhong Plain. *Remote Sens.* **2016**, *8*, 690. [[CrossRef](#)]
59. Wu, H.; Adler, R.F.; Tian, Y.; Huffman, G.J.; Li, H.; Wang, J. Real-time global flood estimation using satellite-based precipitation and a coupled land surface and routing model. *Water Resour. Res.* **2014**, *50*, 2693–2717. [[CrossRef](#)]
60. Ullah, I.; Ma, X.; Asfaw, T.G.; Yin, J.; Iyakaremye, V.; Saleem, F.; Xing, Y.; Azam, K.; Syed, S. Projected Changes in Increased Drought Risks Over South Asia Under a Warmer Climate. *Earth's Future* **2022**, *10*, e2022EF002830. [[CrossRef](#)]
61. Ullah, I.; Saleem, F.; Iyakaremye, V.; Yin, J.; Ma, X.; Syed, S.; Hina, S.; Asfaw, T.G.; Omer, A. Projected Changes in Socioeconomic Exposure to Heatwaves in South Asia Under Changing Climate. *Earth's Future* **2022**, *10*, e2021EF002240. [[CrossRef](#)]
62. Hassan, M.; Du, P.; Mahmood, R.; Jia, S.; Iqbal, W. Streamflow response to projected climate changes in the Northwestern Upper Indus Basin based on regional climate model (RegCM4.3) simulation. *J. Hydro-Environ. Res.* **2019**, *27*, 32–49. [[CrossRef](#)]
63. Iyakaremye, V.; Zeng, G.; Ullah, I.; Gahigi, A.; Mumo, R.; Ayugi, B. Recent Observed Changes in Extreme High-Temperature Events and Associated Meteorological Conditions over Africa. *Int. J. Climatol.* **2022**, *42*, 4522–4537. [[CrossRef](#)]
64. Wu, J.; Chen, X. Spatiotemporal trends of dryness/wetness duration and severity: The respective contribution of precipitation and temperature. *Atmos. Res.* **2019**, *216*, 176–185. [[CrossRef](#)]

65. Wu, J.; Chen, X.; Yu, Z.; Yao, H.; Li, W.; Zhang, D. Assessing the impact of human regulations on hydrological drought development and recovery based on a 'simulated-observed' comparison of the SWAT model. *J. Hydrol.* **2019**, *577*, 123990. [[CrossRef](#)]
66. Lu, K.; Arshad, M.; Ma, X.; Ullah, I.; Wang, J.; Shao, W. Evaluating observed and future spatiotemporal changes in precipitation and temperature across China based on CMIP6-GCMs. *Int. J. Climatol.* **2022**, *42*, 7703–7729. [[CrossRef](#)]

**Disclaimer/Publisher's Note:** The statements, opinions and data contained in all publications are solely those of the individual author(s) and contributor(s) and not of MDPI and/or the editor(s). MDPI and/or the editor(s) disclaim responsibility for any injury to people or property resulting from any ideas, methods, instructions or products referred to in the content.